ORIGINAL ARTICLE

Numerical investigation of the liquid-fueled pulse detonation engine for different operating conditions

V. B. Nguyen[1,2] · C. J. Teo[2,3] · P.-H. Chang[2] · J. M. Li[2] · B. C. Khoo[2,3]

Abstract

In this study, an intensive simulation platform is developed and implemented to simulate the three stages in the operational cycle of the liquid-fueled pulse detonation engine. The three stages encompass the liquid fuel injection and evaporation process, deflagration-to-detonation transition process, and detonation propagation process. The Lagrangian–Eulerian approaches are employed to model the discrete liquid fuel droplets and the continuous vapor phase, respectively. The breakup and evaporation of liquid droplets are modeled using sub-models, while the interactions between the liquid droplets and the vapor phase are expressed through the two-way interaction models. The Jet-A liquid fuel is injected into the detonation chamber as the fuel for the engine, while the air flow is used as the oxidizer. A reduced chemical kinetic model of fuel/air is used to model the combustion process. The simulation platform is systematically validated against the experimental data for every stage of the operating cycle. To study the influence of the inlet and operating conditions, the numerical simulations are performed for three different operating conditions, which are the change in inlet air temperature, the change in inlet air flow velocity, and the change in liquid fuel mass flow rate. The obtained results indicate that the mass fraction of pre-vaporization of fuel plays an important role in the successful DDT process and/or detonation onset. The deflagration can successfully transit to detonation for both the cases of complete and incomplete vaporization of the liquid droplets inside the detonation chamber. The deflagration cannot successfully transit to detonation for the case of too lean or too rich fuel vapor in the mixture. The calculated burning temperature and Chapman–Jouguet (C–J) detonation velocity are slightly lower in the cases of the incomplete vaporization when compared to the complete vaporization cases. In addition, our numerical results show that the burning process occurs in two stages in the incomplete vaporization case: The first burning stage plays a main role in the successful DDT process, while the second burning stage only plays the role of augmentation.

Keywords Liquid-fueled PDE · Evaporation · Deflagration-to-detonation transition · Pulse detonation engines

1 Introduction

In pulse detonation engine (PDE) development and operation, the use of liquid fuel is always of interest due to its advantages, such as higher energy density, ease of storage,

smaller storage tank, simpler storage systems, and safer handling compared to the gaseous fuel [1]. As such, the total weight and volume of the flight device can be reduced. The greater energy density of the liquid fuel can provide more power to the propulsion system. Due to the high potential benefit of implementation, numerous investigations of liquid-fueled detonation engines have been carried out for both the experimental and numerical studies [2–15]. In particular, for experimental investigation, Webber [2] and Crammer [3] conducted research on spray detonations for a liquid-fueled rocket engine. Ragland et al. [4] experimentally observed the structure of spray detonations. They suggested that the difference in the detonation velocity observed is caused by friction and heat transfer losses. Dabora et al. [5] carried out experiments to investigate the effect of the droplet size on the detonation properties (e.g., detonation wave propagation

✉ V. B. Nguyen
nguyenvb@ihpc.a-star.edu.sg

[1] Fluid Dynamic Department, Institute of High Performance Computing, Singapore 138632, Singapore

[2] Temasek Laboratories, National University of Singapore, Singapore 117411, Singapore

[3] Department of Mechanical Engineering, National University of Singapore, Singapore 119260, Singapore

velocity, velocity deficit, etc.). They concluded that the detonation propagation velocity is generally lower than the ideal C–J velocity in the gaseous phase. Furthermore, Bull et al. [6] performed experiments to study the detonation of unconfined fuel/air aerosol for both low- and high-vapor-pressure fuels for a wide range of liquid fuel droplets up to 100-μm-sized droplets. They found that a certain quantity of the fuel vapor prior to ignition might be required for self-sustained detonation propagation. In addition, Brophy et al. [7] studied the detonability limits of JP-10/air to characterize the mixture with respect to the droplet size, temperature, and level of pre-vaporization. They also suggested that a significant amount of initial fuel vapor would be required for detonation onset. In particular, a spray detonation was attained in the PDE when the inlet air temperature was greater than 102 °C (375.15 K) with the support of a pre-detonator. For the lower temperature, the sustained detonation required 70% of the fuel to be evaporated and liquid droplet sizes smaller than 3 μm. To attain the necessary pre-vaporization fuel level, Frolov [8] and Fan et al. [9] conducted experiments on the DDT process by starting from room temperature and found the tube temperature that was deemed favorable for the liquid-fueled PDE, while Schauer et al. [10] and Tucker et al. [11] demonstrated an operational PDE of up to 15 Hz with the inlet air heated to the temperature of 123 and 149 °C (396.15 and 422.15 K), respectively. Recently, Li et al. [12] have performed a series of experiments on excessively fuel-rich conditions for cold-starting the liquid-fueled pulse detonation engine to establish the criteria for detonation transition of two-phase mixtures based on the PDE filling time and droplet life time, leading to a range of appropriate PDE operating parameters, such as droplet size, inlet air temperature, and PDE running frequency. They also concluded that successful detonation experiments using liquid fuels can be generally achieved when the vapor phase equivalence ratio is near-stoichiometric or slightly fuel rich.

In a theoretical and numerical investigation, Williams [13] developed the one-dimensional ZND detonation model for spray detonations. He reported that the size of the burning region is about the order of a meter as the radius of the droplet spray stays about 30 μm. Borisov et al. [14] numerically studied the effect of the droplet stripping, shattering, and deformation on detonation characteristics with respect to the droplet size. Burcat and Eidelman [15] numerically studied the evolution of the detonation in a cloud of fuel droplets. They reported that the CJ detonation velocity is achieved as the average diameter of droplet size stays smaller than 100 μm, while the detonation velocity is inversely proportional to the reaction zone for larger droplet size. Moreover, Chang and Kailasanath [16] found that the attenuation of shock waves by a dispersed phase is increased when the liquid droplet breakup and vaporization are included. They commented that to establish the liquid-fueled detonation,

the effect of the energy release must continuously overcome the attenuation effects. Subsequent to that, Cheatham and Kailasanath [17] developed a numerical model for liquid-fueled pulse detonation engines based on Eulerian–Lagrangian approaches with a two-way coupling interaction model. Their results show that the detonation structure is varied with the initial droplet size and the amount of the initial fuel vapor present. They also concluded that the smaller the droplet size, the greater the level of heating, and pre-vaporization is shown to enhance transition to a sustained detonation. In general, although numerous studies in both the experimental and numerical areas have been accomplished for the liquid-fueled detonation, a greater understanding of both the physical and chemical insights of a complete operating cycle of the liquid-fueled detonation engine is still lacking. Issues to be considered are: how the inlet and/or operating conditions influence the injection and vaporization process; the effect of the dynamics of the injection and vaporization process on the DDT process; interaction between the liquid droplets and flames, shock waves, and detonation waves; and the role of the pre-vaporization on the DDT process, etc.

In real applications, liquid fuels, often used in the propulsion system, are jet fuels (e.g., Jet-A, Jet-A1, JP-10, kerosene, etc.). The use of a liquid fuel often involves many other sub-processes and is much more complex as compared to the simpler, pure gaseous fuel (e.g., liquid injection, multiphase flow, evaporation, atomization, breakup, chemical mixing, heat transfer between liquid droplet and vapor phase, etc.). To gain further understanding of the dynamics of all processes involved and linked to each other in the operating cycle of the detonation engine, as well as to improve the performance characteristics of the pulse detonation engine, it is therefore deemed necessary to study (and incorporate in simulations) each process in somewhat greater detail. In fact, a complete operating cycle of the detonation engine often involves three main processes: the injection and vaporization process, the deflagration-to-detonation transition process, and the detonation propagation process. Each of the sub-processes can be found in the published literature, such as atomization and droplet size effects [5], heat transfer [4], turbulence-chemistry mixing [18], evaporation process [19], incomplete reaction and reaction beyond the C–J plane [20], excessive fuel-rich conditions for cold-starting [12], and others, which are required in the three main processes in order to elucidate better and clearer physical and chemical insights of the complete operating cycle of a liquid-fueled detonation engine.

In this study, a numerical simulation platform is developed and implemented to simulate the liquid-fueled pulse detonation engine. In particular, the Eulerian–Lagrangian formulation is employed in the numerical models [21]. The continuous vapor phase is modeled using the reacting flow Navier–Stokes equations and described in the Eulerian

frame of reference, while liquid fuel droplets are treated as a discrete phase and expressed in the Lagrangian frame of reference. The two-way interaction between liquid droplets and vapor phase (heat transfer, mass transfer, drag, etc.) and sub-processes (evaporation, breakup, etc.) are modeled and implemented in the simulation platform. Three different sets of operating conditions are used in the simulations to study the coupled dynamics of three main processes of the complete operating cycle of the PDE. The rest of this paper is organized as follows: Sect. 2 introduces the mathematical and numerical models, Sect. 3 presents the validations of the simulation platform, Sect. 4 shows the numerical setup of the different operating conditions, Sect. 5 shows the relevant results and discussions, and finally Sect. 6 concludes with the main findings.

2 Mathematical model and numerical approaches

In this study, we shall assume that the system contains both the vapor phase and the liquid fuel droplet phase. The Eulerian–Lagrangian approach is employed. The continuous vapor phase (or gas mixture) is described using the Reynolds-averaged Navier–Stokes equations (RANS) and expressed in the Eulerian frame of reference, while the discrete liquid droplets (liquid fuel spray) are expressed in the Lagrangian frame of reference. The liquid fuel is injected into the detonation chamber through the slit nozzle. The temperature is uniform inside each liquid fuel droplet. The Ranz–Marshall heat transfer model [22, 23] is used to account for the heat transfer between the liquid fuel droplet and the surrounding gas. This model is based on the convective heat transfer of the droplet with uniform temperature and equal to its surface temperature. Also, we shall assume that the droplets are spherical in shape; therefore, the momentum transfer obeys the spherical law [24]. The evaporation followed the empirical D^2-law model for the fuel used [25]. Finally, the chemical reactions only occur in the gas (vapor) phase. The combustion process of the Jet-A fuel and air is modeled using a reduced chemical kinetic model [26]. Following are the governing equations and numerical methodologies, which are employed to systematically model the liquid-fueled pulse detonation engine.

2.1 Governing equations for vapor phase

Mathematically, we assume that all species in the gas mixture are thermally perfect and the applicability of the EOS (equation-of-state) of the perfect gas. Also, thermal properties of the gas species are functions of temperature, and the system is an adiabatic system with no heat flux through the wall chamber. There is no gravity force acting on the gas

species, but is applied on the liquid fuel droplets. In addition, there is no radiation emitted by liquid fuel droplets to the gas phase. Thus, the conservative equations of density, momentum, energy, and species for the viscous, compressible, and reacting gaseous phase can be described in the Reynolds-averaged Navier–Stokes (RANS) equations as follows:

$$\frac{\partial \bar{\rho}}{\partial t} + \frac{\partial (\bar{\rho}\bar{u}_i)}{\partial x_j} = S_{m,d}, \tag{1}$$

$$\frac{\partial (\bar{\rho}\bar{u}_i)}{\partial t} + \frac{\partial}{\partial x_j}\left(\bar{\rho}\bar{u}_i\bar{u}_j + \frac{2}{3}\delta_{ij}\bar{\rho}k\right)$$
$$= \frac{\partial}{\partial x_j}(\mu + \mu_T)\left(\frac{\partial \bar{u}_i}{\partial x_j} + \frac{\partial \bar{u}_j}{\partial x_i} - \frac{2}{3}\delta_{ij}\frac{\partial \bar{u}_m}{\partial x_m}\right) - \frac{\partial \bar{p}}{\partial x_i} + S_{u,d}, \tag{2}$$

$$\frac{\partial (\bar{\rho}\bar{e}_t)}{\partial t} + \frac{\partial}{\partial x_j}\left((\bar{\rho}\bar{e}_t + \bar{p})\bar{u}_j\right) = \frac{\partial}{\partial x_j}\left(\bar{\rho}(a + a_T)\frac{\partial \bar{h}_t}{\partial x_j} + \bar{\tau}_{ij}\bar{u}_i\right) + S_{e,d}, \tag{3}$$

$$\frac{\partial (\bar{\rho}\bar{Y}_k)}{\partial t} + \frac{\partial}{\partial x_j}\left(\bar{\rho}\bar{u}_i\bar{Y}_k\right) = \frac{\partial}{\partial x_j}\left(\bar{\rho}(D + D_T)\frac{\partial \bar{Y}_k}{\partial x_j}\right) + S_{Y_k,d} + \bar{\omega}_k. \tag{4}$$

In these equations, $\bar{\rho}$ is the density of the gas mixture, $\bar{u}$ is the vector velocity field, μ is the dynamic viscosity, $a = \lambda/\rho c_p$ is the thermal conductivity, D is the gas diffusivity coefficient, $\bar{p}$ is the pressure field, $\bar{e}_t$ is the total energy, and $\bar{Y}_k$ is the mass fraction of species k. μ_T is the turbulent dynamic viscosity, a_T is the turbulent thermal conductivity coefficient, and D_T is the turbulent diffusivity coefficient. Here, $S_{m,d}$ is the source term for the mass transferred from the liquid droplets, $S_{u,d}$ is the momentum exchange between gas phase and liquid droplets, $S_{e,d}$ is the source term for the heat exchange between the liquid droplets and the surrounding gas phase, $S_{Y_k,d}$ is the source term for species k resulting from liquid fuel evaporation, and $\bar{\omega}_k$ is the formation/loss of the gas species k in the gas phase chemical reactions. Details of the source terms in (1–4) can be referred to in the Appendix. The Reynolds stresses are expressed as follows:

$$\bar{\tau}_{ij} = -\bar{\rho}\widetilde{u_i'u_j'} = \mu_T\left(\frac{\partial \bar{u}_i}{\partial x_j} + \frac{\partial \bar{u}_j}{\partial x_i} - \frac{2}{3}\delta_{ij}\frac{\partial \bar{u}_m}{\partial x_m}\right) - \frac{2}{3}\bar{\rho}\delta_{ij}\frac{\widetilde{u_i'u_i'}}{2}, \tag{5}$$

$$\widetilde{\bar{\rho}\bar{h}_t'u_j'} = -\bar{\rho}a_T\frac{\partial \bar{h}_t}{\partial x_j}, \tag{6}$$

$$\widetilde{\bar{\rho}\bar{u}_j'\bar{Y}_k'} = -\bar{\rho}D_T\frac{\partial \bar{Y}_k}{\partial x_j}. \tag{7}$$

For turbulence modeling, the RANS-based turbulence model employed in this work is the k–ω shear–stress transition (SST) model [27]. The SST model combines the standard k–ε model by Launder and Sharma [28] with the k–ω model by Wilcox [29]. The improved near-wall capability of the SST model as compared to the standard k–ε model yields certain benefits in combustion applications that usually feature a central flame zone with high velocities and turbulence and slower flow close to the walls. The near-wall flow and the corresponding boundary layer can be described with a wall function [30]. Following are the transport equations for the k–ω SST model:

$$
\frac{\partial(\bar{\rho}k)}{\partial t} + \frac{\partial(\bar{\rho}uk)}{\partial x_i} = \frac{\partial}{\partial x_i}\left[\left(\mu + \frac{\mu_T}{\sigma_k}\right)\frac{\partial k}{\partial x_i}\right] \\
+ 2\mu_T S_{ij} S_{ij} - \frac{2}{3}\bar{\rho}k\frac{\partial \tilde{u}_i}{\partial x_i}\delta_{ij} - \beta^* \bar{\rho}k\omega,
$$
(8)

$$
\frac{\partial(\bar{\rho}\omega)}{\partial t} + \frac{\partial(\bar{\rho}u\omega)}{\partial x_i} = \frac{\partial}{\partial x_i}\left[\left(\mu + \frac{\mu_T}{\sigma_{\omega,1}}\right)\frac{\partial \omega}{\partial x_i}\right] \\
+ \gamma_2\left(2\bar{\rho}S_{ij}S_{ij} - \frac{2}{3}\bar{\rho}\omega\frac{\partial \tilde{u}_i}{\partial x_i}\delta_{ij}\right) - \beta_2\bar{\rho}\omega^2 \\
+ 2\frac{\bar{\rho}}{\sigma_{\omega,2}\omega}\frac{\partial k}{\partial x_k}\frac{\partial \omega}{\partial x_k}.
$$
(9)

In these expressions, the turbulent kinetic energy $= \frac{\widetilde{u_i' u_i'}}{2}$, while the specific rate of diffusion is $\omega = \varepsilon/k\beta^*$, and $S_{ij} = \frac{\partial \tilde{u}_i}{x_j} + \frac{\partial \tilde{u}_j}{x_i}$. The model constants are $\sigma_k = 1.0, \sigma_{\omega,1} = 2.0, \sigma_{\omega,2} = 1.17, \gamma_2 = 0.44, \beta^* = 0.09, \beta_2 = 0.083$, see Ref. [31].

2.2 Governing equation for fuel liquid droplet

In this study, the liquid fuel is injected into the detonation chamber with the *blob* injection model within OpenFoam [30, 32]. After the release from the nozzle exit, the initial droplets will be formed and then they will travel inside the detonation chamber toward the outlet of the engine. During the travel time (so-called residence time), the injected liquid droplets break up into smaller droplets and exchange their mass, momentum, and energy with the vapor phase. We assume that the volume fraction of the droplets is small compared to the vapor phase so that the droplet–droplet interactions are negligible. These two-way interactions are modeled by a set of sub-models and described in the Lagrangian frame of reference as follows:

$$
\frac{\partial x}{\partial t} = u_d,
$$
(10)

$$
m_d\frac{\partial u_d}{\partial t} = \sum F_i,
$$
(11)

$$
m_d c_{d,s}\frac{\partial T}{\partial t} = h_k A_d\left(T_v - T_d\right) + \sum S_{h,i},
$$
(12)

$$
\frac{\partial m_d}{\partial t} = \sum S_{m,i}.
$$
(13)

In the (10–13), x is droplet position, u_d is droplet velocity, F_i is external forces acting on a droplet (e.g., drag force, gravity force, and pressure gradient force), h_k is the heat transfer coefficient between vapor phase and liquid droplet, A_d is the contact area (droplet surface area), T_d is droplet temperature, and T_v is the surrounding vapor phase temperature. Here, $\sum S_{h,i}$ is the heat transfer source term between liquid droplets and surrounding vapor phase, and $\sum_i S_{m,i}$ is the mass transfer in the evaporation process, which is determined from the conservation of mass for the fuel. Similarly, these numerical source terms (sub-models) are also described in the Appendix.

2.3 Chemical kinetic model and combustion model

As mentioned in the previous section, the chemical kinetics is comprised of the reduced chemical kinetic model of Jet-A fuel/air mixture, which is proposed in [26]. In this model, the surrogate fuel is represented by species $C_{11}H_{21}$. The model involves 18 chemical reactions of 15 species. The reader is referred to the study [26] for more details. The thermal properties (e.g., specific heat constant (C_p), enthalpy (h), Gibbs energy [33]) of each species and mixture are computed using the NASA polynomial functions with seven coefficients that are obtained from the Chemkin II database [33]. The transport coefficients (dynamic viscosity, kinematic viscosity, and thermal conductivity) are determined using the Sutherland correlation [34]. In this study, the Prandtl number is set at 0.71 for all simulations. This chemical kinetic model has been validated against the experimental data for ignition time, laminar flame speed, and adiabatic temperature. The complete reduced chemical kinetic mechanism is shown in Table 1. The Arrhenius reaction rate coefficient is determined as $k = A\left(\frac{T}{T_0}\right)^n \exp\left(-\frac{E}{RT}\right)$ with units of mol/cm^{-3} s. In this expression, A is the pre-exponential factor, n is the temperature exponent, E is the activation energy (cal/mol), T is the current mixture temperature (K), R is the universal gas constant, and T_0 is the reference temperature (K). Species M is used to account for the effect of third body reactions.

For the combustion modeling, the partially premixed mixture approach is employed to model the combustion process via the reaction progress variable ($c(x, t)$) [35, 36]. The transport equation for the reaction progress variable is given as:

$$
\frac{\partial(\rho c)}{\partial t} + \frac{\partial(\rho c u)}{\partial x} = \frac{\partial}{\partial x}\left(\rho D_{eff}\frac{\partial c}{\partial x}\right) + \omega_{c,def} + \omega_{c,ign}.
$$
(14)

In this approach, the transport equation (14) is solved numerically instead of the stiff ODEs system for all species. The values of all species are pre-computed and tabulated,

Table 1 Reduced chemical kinetic mechanism for Jet-A surrogate fuel (mol/cm^{-3} s)

No.	Reaction	A	n	E
1	$C_{11}H_{21} + O_2 \rightarrow 11CH + 10H + O_2$ Forward/$C_{11}H_{21}$ 0.8/ Forward/O_2 0.8/	1.00E+12	0.00	3.10E+04
2	$CH + O_2 \rightarrow CO + OH$	2.00E+15	0.00	3.00E+03
3	$CH + O \rightarrow CO + H$	3.00E+12	1.00	0.00E+00
4	$H_2 + O_2 \leftrightarrow H_2O + O$	3.98E+11	1.00	4.80E+04
5	$H_2 + O \leftrightarrow H + OH$	3.00E+14	0.00	6.00E+03
6	$H + O_2 \leftrightarrow O + OH$	4.00E+14	0.00	1.8E+04
7	$H_2O + O_2 \leftrightarrow 2O + H_2O$	3.14E+12	2.00	1.12E+05
8	$CO + OH \leftrightarrow CO_2 + H$	5.51E+07	1.27	−7.58E+02
9	$CO + H_2O \leftrightarrow CO_2 + H_2$	5.50E+04	1.28	−1.00E+03
10	$CO + H_2 + O_2 \leftrightarrow CO_2 + H_2O$	1.60E+14	1.60	1.80E+04
11	$N + NO \leftrightarrow N_2 + O$	3.00E+12	0.30	0.00E+00
12	$N + O_2 \leftrightarrow NO + O$	6.40E+09	1.00	3.17E+03
13	$N + OH \leftrightarrow NO + H$	6.30E+11	0.50	0.00E+00
14	$N + N + M \leftrightarrow N_2 + M$	2.80E+17	−0.75	0.00E+00
15	$H + N_2O \leftrightarrow N_2 + OH$	3.50E+14	0.00	7.55E+02
16	$N_2 + O_2 + O \leftrightarrow N_2O + O_2$	1.00E+15	0.00	3.02E+02
17	$N_2O + O \leftrightarrow 2NO$	1.50E+15	0.00	3.90E+04
18	$N_2O + M \leftrightarrow N_2 + O + M$	1.16E+15	0.00	3.32E+04

The third body (M) coefficients in reaction 14 and reaction 18 are 1.0 and 1.0, respectively

which are selected based on the calculated value of $c(x,t)$. In particular, the value of the reaction progress variable is $0 \leq c(x,t) \leq 1$, where c = 0 represents the unburnt mixture and $c = 1$ represents the completely burnt mixture. Equation (14) contains two source terms that account for the deflagrative ($\omega_{c,\text{def}}$) and detonative combustion ($\omega_{c,\text{ign}}$), respectively. The deflagrative source term ($\omega_{c,\text{def}}$) is modeled using the combustion model of Weller [37], while the detonation source term ($\omega_{c,\text{ign}}$) is clearly described in [21, 38]. Kindly refer to [21, 38] for more details of the combustion model for the pulse detonation engine.

2.4 Numerical approach

A complete cycle of the liquid-fueled pulse detonation engine includes three stages: injection and evaporation process (stage 1), deflagration-to-detonation transition process (DDT) (stage 2), and detonation wave propagation process (stage 3). The injection and evaporation process is modeled using the injection model, breakup model, drag model, heat transfer model, and evaporation model. Stage 1 starts from the time as the first droplet is injected into the detonation chamber to the time when the fuel vapor reaches the outlet of the detonation chamber. When stage 1 is completed, a small hot spot with high temperature is introduced at the ignition region to start the flame for the DDT process. At the beginning of stage 2, a laminar flame is formed and starts propagating at a low speed; it accelerates along the

detonation tube, then shock waves and local hot spots are formed, and detonation waves are formed. Stage 3 starts when the detonation waves are formed and start propagating toward the outlet of the chamber. Stage 3 will finish when detonation products move out from the detonation outlet. Figure 1 shows a schematic diagram of a complete liquid-fueled detonation cycle:

As mentioned in the previous section, the Eulerian and Lagrangian numerical approaches are employed to model the continuous vapor phase and discrete liquid droplet phase, respectively. In the Eulerian approach, the governing equations of the gas mixture (1–4) are solved using a finite volume method by taking the integrations over the control volumes. In particular, the computational domain is spatially discretized into small control volumes. At every control volume, the discretization of the governing conservative formulations can be formulated for the divergence, gradient, and Laplace operators, time-discretization, and source terms. The density-based solver, developed in OpenFoam [30], is used to solve for the discretization form of the unsteady, compressible, viscous, and reacting Reynolds-averaged Navier–Stokes equations. The convective flux terms are computed using the second-order HLLC scheme [39] with the slope limiter used in [40]. In fact, the HLLC scheme is suitable for simulating a high-speed compressible flow, as well as the presence of shock waves in the DDT and detonation problem. Since the HLLC scheme might not be economical for the low Mach number flow regime, the

Fig. 1 Schematic diagram of the complete numerical liquid-fueled detonation cycle
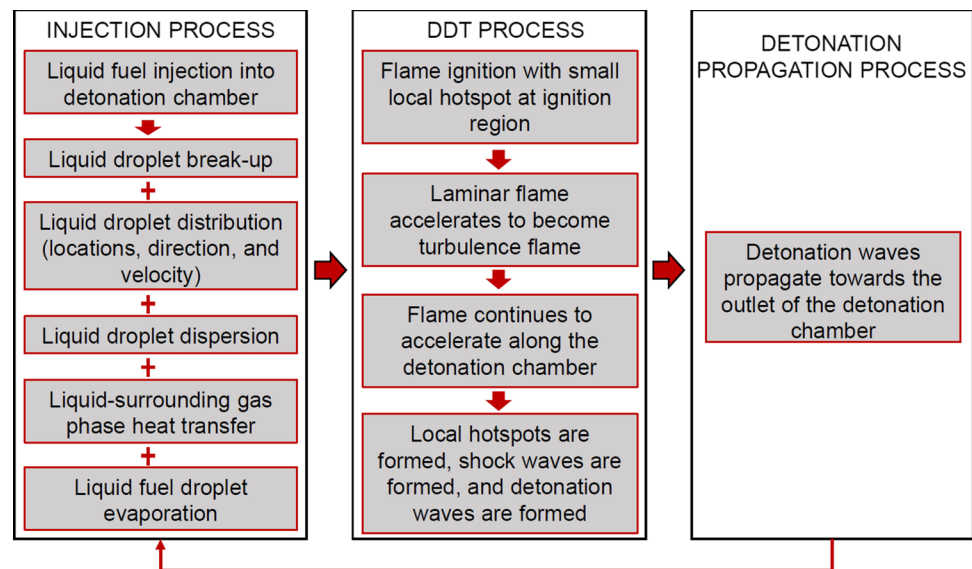
Pressure Implicit with Splitting of Operator (PISO) solver [30] is employed instead to handle the low-speed flow in stage 1 and stage 2. To ensure the governing equations are conservative, the numerical source terms are added into the corresponding discretized equations in the implementation of the PISO solver [38]. As such, the effects of the non-conservative formulation of the Navier–Stokes equations, which are inherited from the pressure-based solver, can be treated. When the velocity is high (Mach number > 0.3), and the compressibility effect is significant, as well as when the combustion-induced flow has been developed, the numerical scheme will switch from the PISO solver to the density-based solver for better shock capturing and inclusion of compressibility effects. In both the PISO solver and the density-based solver, the solution is advanced in time using the transient, second-order Euler implicit scheme.

In the Lagrangian approach, the governing equations for the liquid droplets are also solved in the discretized form. The standard semi-implicit Euler method is used to advance the Lagrangian solution in time [30]. The Lagrangian solution is updated at every time step of solving the Eulerian flow field variables. When the time step, Δt, of the flow variables is large and the computational cell (control volume) size is small, a liquid droplet can travel through several computational cells within a single time step. Thus, to improve the numerical accuracy, the time step (Δt_d) size of the droplet is split into smaller time steps using the adaptive time step size method. As such, all the source terms of the liquid droplet can be evaluated accurately at every computational cell, where the droplet passes through. Alternatively, the interpolation method is adopted to evaluate for the source terms of the liquid droplet at every computational cell along its trajectory as the small time step of Δt_d is still not sufficient. The fact

that the number of liquid droplets in the spray is often very large necessitates significant computational resources and time to compute. Thus, in order to save computational time and computer resources efficiently, the liquid droplets with identical parameters are grouped into a small group (so-called computational parcel) to compute together in a single parcel [30].

For the boundary conditions of the Eulerian variables, at the inlet boundary, the temperature and mass flow rate of the airflow are specified, while Neumann boundary conditions are applied to all other variables. At the solid wall, the non-slip and reflective boundary conditions are specified for the velocity field, the adiabatic boundary condition is applied on the temperature, and all other variables are defined using Neumann boundary conditions. At the outlet of the detonation chamber, the non-reflected outflow boundary condition is applied on the velocity field, and the pressure field is specified together with the transmissivity pressure wave to treat the compressibility effects and supersonic outflows. For the boundary conditions of the Lagrangian variables, the rebound velocity model is utilized for the velocity of the liquid droplet when it impinges on the solid wall, and the *escape* boundary condition is applied on the liquid droplets when they move out from the outlet of the detonation chamber [30]. The rebound boundary condition is defined as $u_{rebound}/u_{in} = e$. Here, u_{in} is incoming velocity just before the impact on the solid wall, $u_{rebound}$ is the rebounding velocity just after the impact, and e is the rebound coefficient that is mainly dependent on surface roughness and the material properties of the surface. If $e = 0$, the liquid droplet adheres to the wall chamber, while if $e = 1$, the liquid droplet rebounds back to the chamber with the same magnitude of the incoming velocity.

For the source terms, the numerical solver is designed to maximize the numerical stability. It is necessary because the coupling of equations for the continuous gas phase and the discrete liquid droplet phase, which are realized via source terms, can lead to instability problems. Here, the interaction between the liquid droplet and continuous gas phase are numerically determined through the particle-source-in-cell method [41], which identifies the cell that the droplet is located in and sets the source terms in the fluid transport equations and corresponding source terms in the balance equations of the liquid droplet. The coupling of gas phase and liquid droplet is thus defined by the values of these source terms. The effect of the liquid droplet (or presence of liquid droplet) is negligible if the liquid droplets are highly dispersed. Details of the numerical source terms are described in the Appendix.

3 On the validation of the simulation platform

In this section, the numerical simulation platform is validated by comparing with the relevant experimental data, which include the experimental data from Sandia National Laboratory [42] for fuel injection and evaporation, our experiments on the fuel injection with slit nozzle, its pattern, and spray angle, and our experiments on the liquid-fueled pulse detonation engine for the flame propagation velocity, run-up distance, and CJ detonation velocity. The experimental descriptions, numerical setups, and comparisons are described below.

3.1 Experimental description

Three experiments used to validate our simulation platform are (C1) experiment on the injection of hexane liquid fuel through the cone injection nozzle carried out by Sandia National Laboratory [42] to compare the results of liquid penetration, vapor penetration, and vapor mass fraction at various stand-off distances; (C2) experiment on the spray pattern of the Jet-A1 liquid fuel through the slit nozzle (it is used in our experiments with the liquid-fueled PDE); (C3) experiment on the DDT process of the liquid PDE using Jet-A fuel to validate for flame speed, run-up distance, and CJ detonation velocity.

In the experiment of Sandia Laboratory [42] (C1), a hydro-eroded nozzle with the inner diameter of 90 μm was used to inject the liquid fuel of N-dodecane ($NC_{12}H_{26}$) into the test chamber with no oxygen to ensure the validity of the no chemical reaction assumption (or no combustion process assumption). The liquid fuel was injected into the test chamber at temperature of 900 K and pressure of 6 MPa for a duration of 1.5 ± 0.001 ms. The ambient gas was nitrogen

with a density of 22.8 kg/m^3. The injection pressure was 150 ± 0.6 MPa, while the injected fuel temperature was about 363 ± 3 K. The total injected mass was 2.5 mg with the square shape of injection rate. The nozzle k factor was 1.5, while the discharge coefficient was 0.86. The experiment was performed to measure the liquid penetration length, vapor penetration length, and the vapor mass fraction at the stand-off distances of 25 and 45 mm. The accuracy of the penetration length measurement is ± 0.29 mm.

In our experiment (C2), the slit nozzle with the thickness of 0.13 mm and the width of 1.3 mm was employed to inject the liquid Jet-A fuel into the test chamber at a temperature of 306 K (or 33 °C) and ambient pressure of 1.0 bar (or 0.1 MPa). The injection pressure was 60.0 bars (or 6.0 MPa), and the fuel injection temperature was 300 K. The total liquid fuel mass of about 13.3 mg was injected for the duration of 0.12 s. The obtained experimental results of spray pattern and angle were then used to validate the numerical simulation platform. The accuracy of the spray angle measurement is $\pm 1.5°$. (It may be noted that this slit nozzle was used in our experiments of the liquid-fueled pulse detonation engine.)

Finally, in our liquid-fueled pulse detonation engine experiment (C3), the engine, with an installed section of a DDT-enhancement device designed with 20 orifice plates and six layers of vortex generation, is tested to measure the flame speed along the tube, DDT run-up distance, and C–J detonation velocity. A schematic design of our liquid-fueled PDE is shown in Fig. 2. In particular, the inner diameter of the PDE tube was 62.7 mm and the total length was 2135.0 mm (from the initiation sparking point to the outlet). The blockage ratio of the orifice plates was 43%. At the ignition section, four Denso automobile spark plugs were securely attached to start the flame. The energy levels from these spark plugs were about 120–150 mJ per spark, as provided by the manufacturer. There were two manifolds connected to the PDE inlet section for filling the air through the engine. A Denso slit nozzle was mounted at upstream of the spark plugs to inject the liquid fuel to the chamber. The electric air heater (Osram Sylvania 48 kW) was employed to heat up the incoming airflow before mixing with liquid fuel and entering the detonation chamber. The static pressure transducer (Kulite) and the Omega k-type thermocouple were installed in a sonic nozzle to quantify the air mass flow rate. The uncertainty of the incoming air flow rate was about 0.886%. The air flow rate could be adjusted by the total pressure of the air supply via the ER3000 pressure controller. For different experiments, the airflow velocity could be adjusted in accordance with the injection time (filling time) of the fuel to ensure that the detonation chamber was entirely filled with fuel vapor at each operating cycle, even for different operating frequencies. The LabVIEW and National Instruments PXI system were used to control
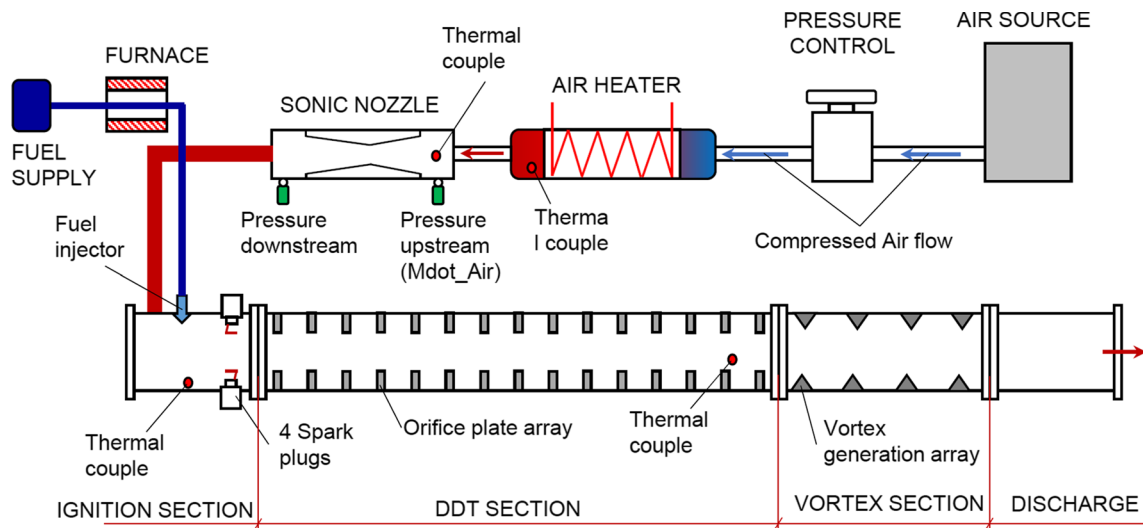
Fig. 2 Schematic design of valveless liquid-fueled pulse detonation engine

the test procedure and data acquisition. Eight piezoelectric pressure transducers (PCB 112A05) and eight in-house ion probes were mounted along the streamwise direction to estimate the propagation velocities of the pressure waves and combustion wave, respectively. The accuracy of the propagation speed measurement was 1.9–5.7%. In this case, the airflow into the chamber was set at the velocity of 35 m/s and temperature of 343 K (about 70 °C) to mix with liquid fuel droplets. The mass flow rate of the liquid fuel (about 2.46 g/s) was injected to maintain the equivalence ratio of fuel/air mixture at about 1.1. The uncertainty of the liquid fuel injection was 0.9%. The injection pressure was 70 bars (or 7 MPa), while the fuel injection temperature was about 300 K. The experiment was carried out for cycle frequency of 2 Hz for the entire 5 s.

3.2 Numerical setup

In order to benchmark with the corresponding experimental sets, the numerical simulations were set up and performed as follows. To validate the Sandia experiment [42] (C1), a 3-D computational domain (a cylinder) was employed. The cylinder with radius of 200 mm and length of 400 mm was created to ensure that the wall boundary conditions were not affecting the spray pattern. The mesh grid size was set at $\Delta r = \Delta z = 0.05$ mm for spatial discretization. The nozzle was modeled as a hollow cone nozzle with the blob disk injection model, which has the same inner diameter of the nozzle used in the experiment (90 µm). The turbulence was modeled using the k–ω SST model. The atomization was modeled using the LISA model. The breakup model was the Kelvin–Helmholtz–Rayleigh–Taylor (KH–RT) model. The drag force made use of the standard spherical drag model.

The D^2-law model was employed for the evaporation process. The time step size of 5.0×10^{-7} s was set for the temporal discretization of the simulation. On the boundary conditions, the wall boundary conditions were employed at all the boundaries; there was no-slip wall boundary condition for the velocity, while the zero gradient was set for pressure and all species, and an isothermal wall was set for temperature. Other initial, operating, and boundary conditions were set similar to the experiment. The comparison results are shown in the next subsection.

To benchmark with the experimental results of the slit nozzle (C2), the numerical simulations were set up and performed as follows. A slit nozzle with thickness of 0.13 mm and the width of 1.3 mm with multiple injection points was modeled in our simulations. The computational domain was a cylinder with radius of 300 mm and length of 800 mm. The nozzle was placed at the top center of the computational domain. The minimum mesh grid size was set at $\Delta r = \Delta z = 0.05$ mm for spatial discretization at the center of the chamber. The mesh grid size was denser at the center of the cylinder and coarser outwards (with the growth factor of 1.1), which was chosen from the preliminary grid convergence study. The injection pressure was setup at 60.0 bars (or 6.0 MPa), while the temperature was 306 K, similar to the experiment. The injection time was 0.12 s. The outflow boundary conditions were set for the velocity at all boundaries. The zero-gradient boundary condition was set for pressure, temperature, and all species at all boundaries. The escape boundary conditions were set for the liquid droplets at all boundaries. The time step size was fixed at 1.0×10^{-6} s. Similarly, the turbulence model is k–ω SST. The atomization was the LISA model. The breakup model was Kelvin–Helmholtz–Rayleigh–Taylor model. The drag force made use of

the standard spherical drag model. The D^2-law model was used for the evaporation process. The initial condition and operating conditions were similar to the related experiment. The comparison of the numerical results of spray pattern and angle with experimental results is shown in next subsection.

Finally, to validate the capability of the simulation platform in modeling DDT and the detonation propagation process in a liquid-fueled PDE (C3), the geometry model of the detonation chamber was created in 2D, which was based on the geometry used in our experiments (3D). Thus, all the values and operators in 3D were interpolated to 2D. The details of the simulated geometry model are shown in Fig. 3. The mesh grid size was chosen from a preliminary mesh grid convergence study with $\Delta x = \Delta y = 0.025$ mm. The Jet-A liquid fuel at a temperature of 300 K was injected into the detonation chamber at the ambient pressure of 1.0 bar (or 0.1 MPa) to mix with the airflow at an incoming velocity of 35 m/s. The incoming airflow was preheated to the temperature of about 343 K (70 °C). The mass flow rate of the liquid fuel was set at 2.46 g/s to attain a global fuel/air equivalence ratio of about 1.1. For the boundary conditions, the mass flow rate and fixed temperature boundary conditions were applied at the inlet, the no-slip and exothermal boundary conditions were applied on the wall chamber, and the outflow boundary conditions were applied to the outlet. The duration of the injection time was 0.065 s. The flame was ignited with a small hot spot at a temperature of 2300 K for about 0.1 ms of duration time. The size of the ignition volume and set temperature was equivalent to an energy level, which was about the same as the four spark ignitors employed in the experiment (120–150 mJ). The numerical results of flame speed along the chamber, run-up distance, and CJ detonation velocity are compared to the experiment and are shown in the next subsection.

3.3 Comparison between experimental data and numerical results

For the validation of our numerical simulation platform with the Sandia experiment (C1), the numerical results of liquid penetration, vapor penetration, and fuel vapor mass fraction at some stand-off distances are compared against the experimental data (see Figs. 4, 5, 6). Figure 4 shows the comparison of the liquid penetration, in which the liquid penetration is the length of the spray (i.e., from the nozzle exit to the farthest point of the existence of liquid droplet). It can be seen that the numerical result was slightly lower than the experiment at the first 0.2 ms; it then became quite comparable to the experiment for both the trend and the magnitude. Figure 5 shows the fuel vapor penetration versus the injection time. Similarly, the vapor penetration is the length of the fuel vapor, which is measured from the nozzle tip to the farthest point of the fuel vapor toward the downstream direction. The comparison points out the good agreement with the experimental data in both the trend and the magnitude. Figure 6 shows the comparison of the mass fraction of the fuel vapor along the radial direction from the center outwards at two different stand-off distances of 25 mm and 45 mm. It shows that the numerical results are in relatively good agreement with the experimental data. It is slightly higher than the experimental data at the outer side at the stand-off distance of 45 mm; however, it still concurs pretty well at the center part at this stand-off distance. In general, we can conclude that the numerical simulation
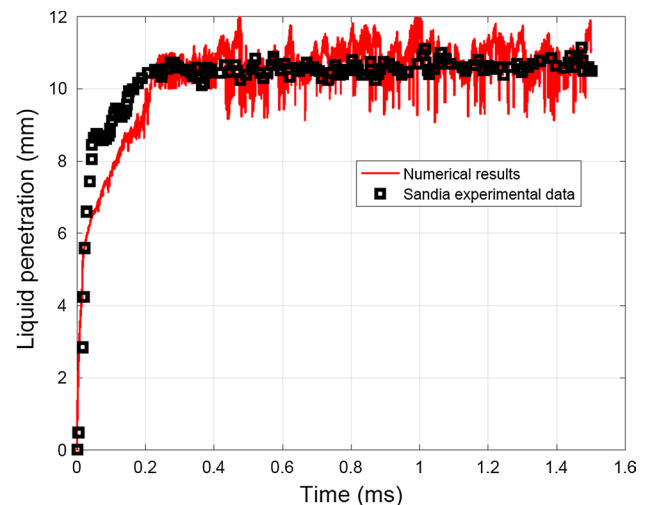

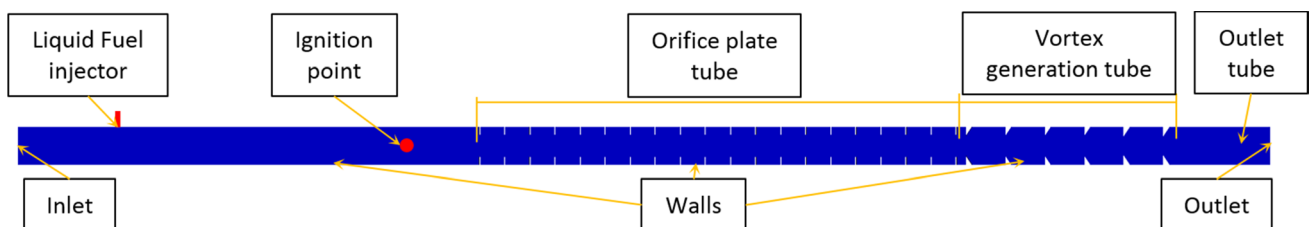**Fig. 4** Comparison of the liquid penetration of the current numerical simulation and Sandia's experimental data
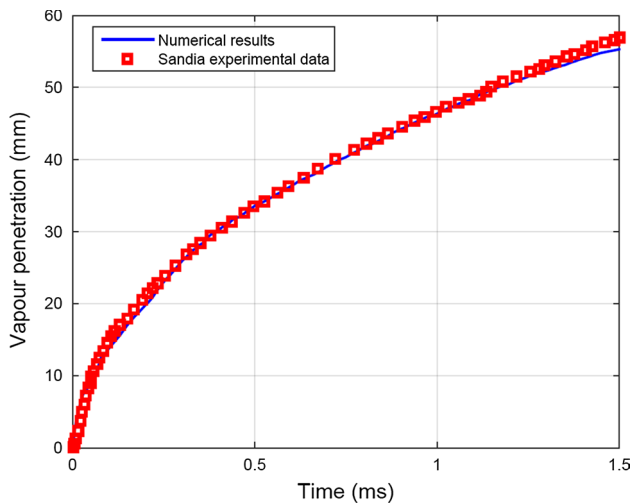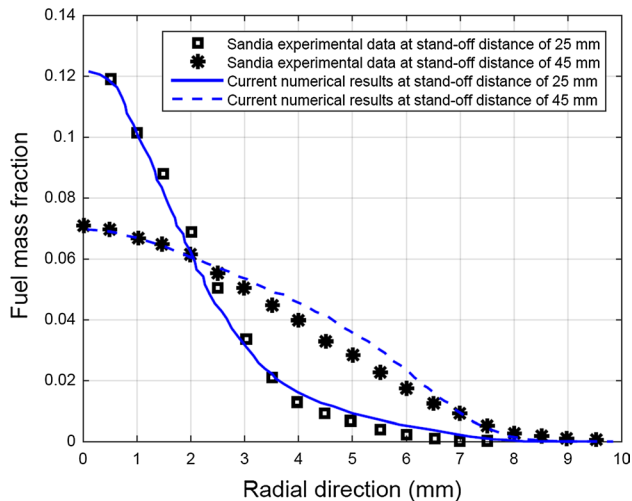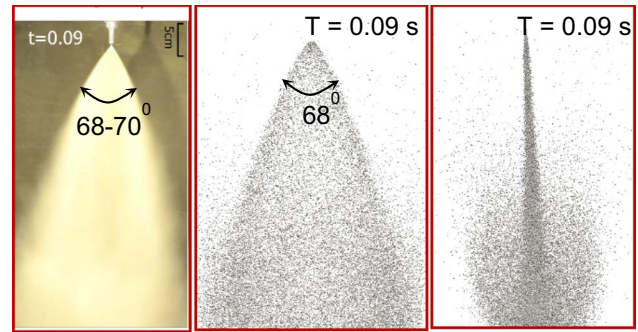

Fig. 3 Geometry model of the detonation chamber

Fig. 5 Comparison of the fuel vapor penetration of the current numerical simulation and Sandia's experimental data

Fig. 7 Comparison of spray pattern between current simulation results and our experimental data at injection time of 0.09 s: **a** front view spray pattern of our experiment, **b** front view spray pattern of current numerical simulation, **c** side view of spray pattern of current numerical simulation
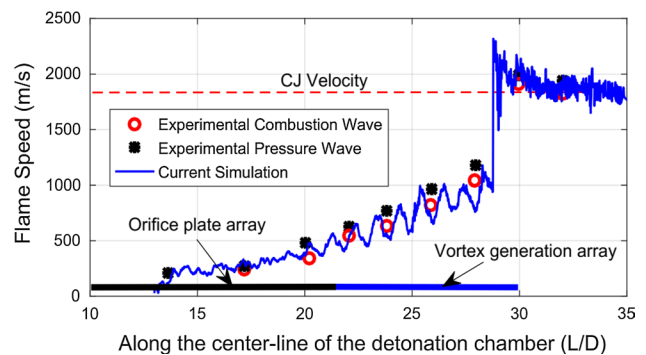

Fig. 6 Comparison of the fuel vapor mass fraction of the current numerical simulation and Sandia's experimental data at stand-off distance of 25 mm and 45 mm

Fig. 8 Comparison of the flame speed along the axis of the detonation chamber between the numerical results and experimental data

platform can favorably perform the experiment with the implemented injection, breakup, drag, heat transfer, evaporation model, etc.

For validation of the numerical simulation platform with the slit nozzle (C2), the numerical results of the spray pattern and spray angle are compared with our experimental data. Figure 7 shows the comparison at the time of $t = 0.09$ s. The left-hand side is the spray pattern of the experimental data, while the middle and right-hand side are the numerical results of the front view and side view of the spray pattern. It can be observed that the spray pattern from the numerical results is comparable to the experiment. The spray angle

of the numerical simulation is about 68° which is consistent with the measurement data of 68°–70°. It can be stated that the simulation platform can reproduce the experimental results of the slit nozzle very well.

Figure 8 shows the comparison of the flame propagation speed of the flame front in the numerical simulation and the pressure wave and combustion wave of the experiment for the same setup and operating conditions. It can be seen that the pressure wave in the experiment propagates slightly faster than the combustion wave and numerical results. However, the averaged values of the numerical results are in good agreement with the combustion wave in the experiment. The DDT run-up distance in the simulation of about $\frac{L}{D} = 28.5$ is comparable to the measurement data of $\frac{L}{D} = 28 - 30$. In addition, the simulation C–J velocity of about 1806 m/s is in good concurrence with the value of 1800 m/s in experiment and published data. In general, comparing the injection, DDT, and detonation process, we can conclude that the implemented simulation platform can favorably simulate the liquid-fueled pulse detonation engine operation.

4 Numerical setup

In this section, numerical simulations that were setup to simulate different operating conditions of the liquid-fueled pulse detonation engine are described. Each case of operating conditions was simulated for the complete operating cycle, which included the injection and evaporation process (stage 1), deflagration-to-detonation transition process (stage 2), and detonation propagation process (stage 3). Similar to the validation section, the 2D geometry model was used to simulate the detonation chamber of 3D in the experiment (see Fig. 3 for more details). The mesh grid size was set similar to the benchmark case with $\Delta x = \Delta y = 0.025$ mm, which was chosen from the preliminary grid convergence study. The boundary conditions were also set similar to the benchmark case in the previous section. The three sets of operating conditions considered were different inlet airflow velocities (OC1), different airflow temperatures (OC2), and different fuel mass fractions (OC3).

The first set of operating conditions (OC1) included five simulations corresponding to the inlet airflow velocity of 12, 16, 18, 27, and 35 m/s. Other conditions were set up similar for all the cases, which were the inlet air temperature of 500 K, temperature of injected liquid Jet-A fuel at about 300 K, the injection pressure at 70 bars (or 7 MPa), and the fuel mass flow rate of 2.5 g/s. At the beginning, the chamber was filled with fresh air at a temperature of 300 K and pressure of 1.0 bar (or 0.1 MPa).

The second set of the operating conditions (OC2) included four simulations corresponding to the incoming airflow temperature of 300, 400, 500, and 600 K. The incoming airflow velocity was set at 35 m/s. Similarly, the liquid Jet-A temperature of 300 K was injected into the detonation chamber at injection pressure of 70 bars (or 7 MPa). The mass flow rate of the liquid fuel was 2.5 g/s. At the beginning, the chamber was also filled with fresh air at a temperature of 300 K and pressure of 1.0 bar (or 0.1 MPa).

The third set of the operating conditions (OC3) included four simulations corresponding to the mass flow rate of the Jet-A liquid fuel of 1.78, 2.67, 3.56, and 4.45 g/s.

The incoming airflow velocity was set at 35 m/s, while the airflow temperature was set at 500 K. Similarly, the liquid Jet-A temperature of 300 K was injected into the detonation chamber at an injection pressure of 70 bars (or 7.0 MPa). And, at the beginning, the chamber was also filled with fresh air at a temperature of 300 K and pressure of 1.0 bar (or 0.1 MPa).

For all cases, a small hot spot with high temperature of 2300 K was used to start the flame at the ignition region. It should be noted that the ignition time must be adjusted to ensure that the flame was formed whether for the case of incomplete vaporization or complete vaporization. The liquid fuel injection time was set based on the incoming airflow velocity to ensure that the entire detonation chamber is filled with fuel vapor. For example, the injection time was about 0.065, 0.08, 0.12, 0.13, and 0.18 s for the airflow incoming velocity of 35, 27, 19, 16, and 12 m/s, respectively. The obtained numerical results are shown and discussed in Sect. 5 below.

5 Results and discussion

In this section, the numerical results of the three set of the operating conditions are reported and analyzed. The salient numerical results for these three sets of operating conditions are summarized in Tables 2, 3, and 4. In particular, the physical and chemical phenomena of the typical cases are carefully analyzed in order to gain a better understanding of the effect of the operating conditions on the three stages. The salient features include the complete vaporization/incomplete vaporization, successful DDT process within the complete/incomplete vaporization, and unsuccessful DDT process.

5.1 Summary of the numerical results

Table 2 shows the numerical results of the set of operating conditions of OC1 (with different inlet airflow velocities). Table 3 shows the numerical results for the set of operating conditions of OC2 (with different incoming airflow temperatures). Table 4 shows the numerical results of the set of operating conditions of OC3 (with different liquid fuel flow

Table 2 Summarized numerical results of the set conditions for different inlet airflow velocities

Inlet air velocity (m/s)	Evaporation process	Vapor mass fraction	T (K) inside chamber	DDT process	C–J vel (m/s)
35	Completed	0.084	430	Successful	1813
27	Completed	0.12	410	Successful	1812
18	Not completed	0.14	390	Successful	1768
16	Not completed	0.145	380	Successful	1758
12	Not completed	0.15	365	Successful	1750

Table 3 Summarized numerical results of the set conditions for different inlet airflow temperatures

T (K) at inlet	Evaporation process	Vapor mass fraction	T (K) inside chamber	DDT process	C–J vel (m/s)
300	Not completed	4.0E−4	300	Unsuccessful	N.A.
400	Not completed	0.06	360	Successful	1797
500	Complete	0.084	425	Successful	1822
600	Complete	0.085	500	Successful	1825

Table 4 Summarized numerical results of the set conditions for different fuel mass flow rates

Mass flow rate (g/s)	Evaporation process	Vapor mass fraction	T (K) inside chamber	DDT process	C–J vel (m/s)
1.78	Completed	0.065	460	Successful	1801
2.67	Completed	0.11	410	Successful	1797
3.56	Not completed	0.13	385	Successful	1776
4.45	Not complete	0.14	380	Successful	1762

rates). In essence, the information on the evaporation process (complete or incomplete vaporization), the average fuel vapor mass fraction, the average temperature of the vapor mixture after the stage 1, the DDT process (successful or unsuccessful transition), and the C–J velocity at the detonation stable state condition are reported in Tables 2, 3, and 4.

In general, for the stage 1, the obtained numerical results show that there is a critical condition at which the evaporation rate reduces to zero (so-called saturation point). This critical condition is influenced by the combination of the inlet airflow temperature, velocity, the injected liquid droplet temperature, and the injected liquid fuel flow rate. Among these parameters, the temperature of both the surrounding vapor mixture and the liquid droplets dominantly influence the evaporation process. For the first set of OC1, the liquid droplets are completely evaporated for the cases of the higher airflow velocities (27 and 35 m/s), while they cannot evaporate completely for the cases with lower velocities (18, 16, and 12 m/s). Because the higher velocity can bring in more airflow at high temperature into the chamber, the heat exchange is the greater and the droplets are evaporated faster. For the second set of OC2, the liquid droplets are completely evaporated for the cases with inlet airflow temperature of 500 and 600 K, while the liquid droplets cannot be evaporated completely inside the chamber for the cases of 400 and 300 K. It is clear that higher temperature of the incoming airflow can make the liquid droplets evaporate faster (and of course inversely). In the third set of OC3, the lesser liquid fuel flow rate injected into the chamber can cause a faster evaporation process (or greater evaporation rate) as the temperature of the surrounding mixture still remains at a greater value, while temperature is brought faster down to a lower value in the cases of higher fuel mass flow rate injected into the chamber, leading to a slower evaporation process. Because the higher mass flow rate of the liquid fuel injected into the domain invariably necessitates more heat of the hot airflow to increase the droplet temperature, the liquid droplets are completely evaporated for the cases of liquid fuel mass flow rate of 1.78 and 2.67 g/s and are not completely evaporated for the cases of liquid fuel mass flow rate of 3.56 and 4.45 g/s.

After stage 1, the results of two parameters (fuel/air equivalence ratio (fuel vapor mass fraction) and the mixture temperature) are very important for the successful DDT process [6–12]. There exists a certain range of pre-vaporization fuel/air equivalence ratio for successful DDT (detonation onset), while too lean or too rich of a fuel vapor mixture can cause failure in the DDT process. Table 2 shows that the fuel vapor mass fraction inside the chamber after stage 1 is greater for the case of lower incoming airflow velocity. The fuel mass fractions are 0.085, 0.12, 0.14, 0.145, and 0.15 corresponding to airflow velocity of 35, 27, 18, 16, and 12 m/s, respectively. This makes sense because in the lower airflow velocity case, both the longer residence time of the droplets and the lower incoming airflow rate mixing gives rise to the fuel mass flow rate being greater. For the OC2, Table 3 shows that vapor fuel mass fraction is higher in the case of higher inlet airflow temperature. The higher temperature causes a faster evaporation rate, which results in a higher fuel vapor mass fraction in the fuel/air mixture for the same residence time of the droplets. The fuel mass fractions are 4.0×10^{-4}, 0.06, 0.085, and 0.085 corresponding to temperatures of 300, 400, 500, and 600 K, respectively. For cases of temperature at 500 K and 600 K, all droplets are completely evaporated so that the average fuel vapor mass flow rate is about the same. The slight difference in fuel vapor mass fraction can be caused by the difference in evaporation rate. For the OC3, Table 4 shows that the fuel vapor mass fraction is greater as the injected fuel mass flow rate is greater. The obtained fuel vapor mass

fractions are 0.065, 0.11, 0.13, and 0.14, which corresponds to the injected fuel mass flow rates of 1.78, 2.67, 3.56, and 4.46 g/s, respectively.

For the liquid-fueled PDE with cold-starting, Li and co-workers [12], based on their experiments, have reported on the relation between the mixture temperature and global equivalence ratio to attain the vapor fuel/air equivalence ratio of about 1.0 to ensure the onset of detonation. In this work, we found that there is a range of the fuel/air equivalence ratio and average mixture temperature where the DDT still successfully transits to detonation (see Tables 2, 3, 4 for details). In fact, the temperature of the mixture after stage 1 is dependent on the heat exchange between the incoming airflow and fuel liquid droplets. For the case of OC1, the longer residence time of liquid droplets and lesser hot airflow rate in the lower velocity case leads to a lower temperature of the mixture (see Table 2 for details). For the case of OC2, the higher temperature of the incoming airflow can bring about a higher temperature of the mixture (see Table 3 for details). For the case of OC3, the higher cold fuel mass flow rate injected has led to the lower temperature of the mixture to reach the energy balance status (see Table 4 for details).

It can be seen that a successful transition of the DDT process to a detonation wave strongly depends on the value of the fuel vapor mass fraction arising from the evaporation process (stage 1). The DDT process cannot successfully transit to a detonation wave if the fuel vapor mass fraction is too low or too high. In this work, the DDT process can successfully transit to detonation as the fuel vapor/air equivalence ratio achieves a value of about 0.8–2.25, even though the global fuel/air equivalence ratio can be very high at up to 4.3. Furthermore, the DDT process also can successfully transit to detonation in both the cases of complete vaporization and incomplete vaporization. In all three sets of operating conditions, the DDT process is only unsuccessful for the case of incoming airflow temperature at 300 K in the set of OC2, while the DDT is successful for all other cases. It can be seen that the fuel vapor mass fraction of the unsuccessful case is too low (about 4.0×10^{-4}). In the detonation onset cases, the C–J detonation velocity was 1800 m/s, which is agreeable with the experimental result and published value for Jet-A fuel. It is also observed that the C–J velocity in the complete vaporization case is only slightly faster than the incomplete vaporization case. (This can be attributed to the detonation wave losing energy to break up and vaporization of the liquid droplets in the unburnt region during the propagation process toward the outlet.)

## 5.2 Insights into the evaporation process

As mentioned in the previous section, the injected liquid fuel droplets are completely evaporated in some cases, while they are not completely evaporated in other cases. The complete or incomplete vaporization process strongly depends on both the evaporation rate of the liquid fuel and the residence time (or travel time) of the liquid droplets inside the detonation chamber. In fact, the evaporation rate and the residence time are functions of the operating conditions and the tube length. Two typical results are analyzed for further understanding (as shown in Figs. 9, 10, 11, 12). In particular, Figs. 9 and 10 show the complete vaporization case (with inlet airflow velocity of 35 m/s, temperature of 500 K, and fuel mass flow rate of 2.5 g/s), while Figs. 11 and 12 show the incomplete vaporization case (with inlet airflow velocity of 35 m/s, temperature of 400 K, and fuel mass flow rate of 2.5 g/s). Analyzing these two typical cases can provide more information related to the evaporation mechanism of the fuel inside the detonation chamber.

Figure 9 shows the temperature contour of the mixture with the existence of the fuel liquid droplets, while Fig. 10 only shows the fuel vapor mass fraction contour. It can be seen that liquid droplets begin vaporizing right after injection into the chamber. The droplets then travel downstream for a short residence time before being evaporated completely. In this case, the liquid penetration length is short. The mixture temperature is lower in the region with the appearance of liquid droplets, and it is higher elsewhere (see Fig. 9a). The fuel vapor mass fraction is locally higher in the region right after the injection point because most of the evaporation process occurs in this region. Under the present detonation chamber structure (with orifice plates and vortex generation), the mixing process makes a more uniform distribution of the fuel and air in the mixture.
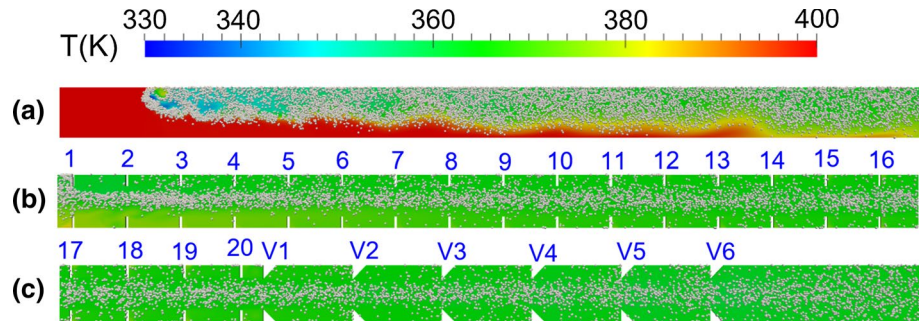

Fig. 9 Complete vaporization case: colored by the temperature contour of the vapor mixture and short appearance of liquid droplets
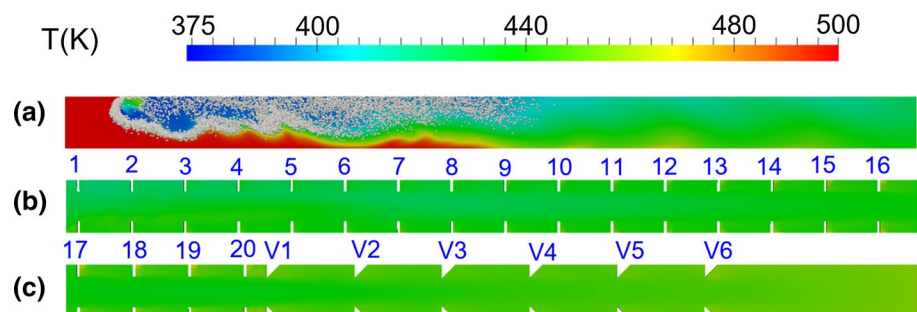
Fig. 10 Complete vaporization case: colored by the mass fraction contour of the fuel vapor
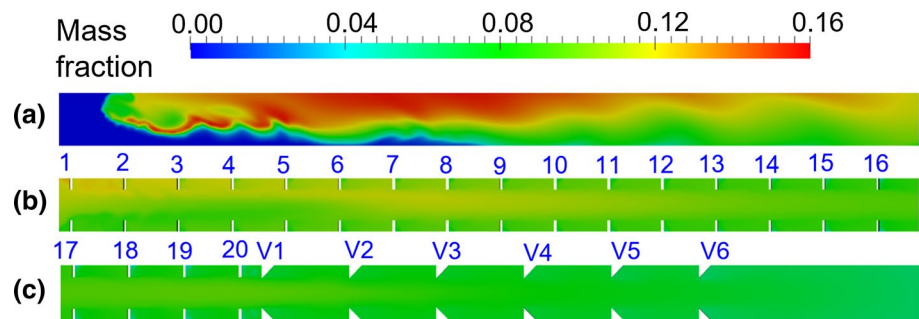
Fig. 11 Incomplete vaporization case: colored by the temperature contour of the vapor mixture and appearance of liquid droplets entire detonation chamber

Fig. 12 Incomplete vaporization case: colored by the mass fraction contour of the fuel vapor
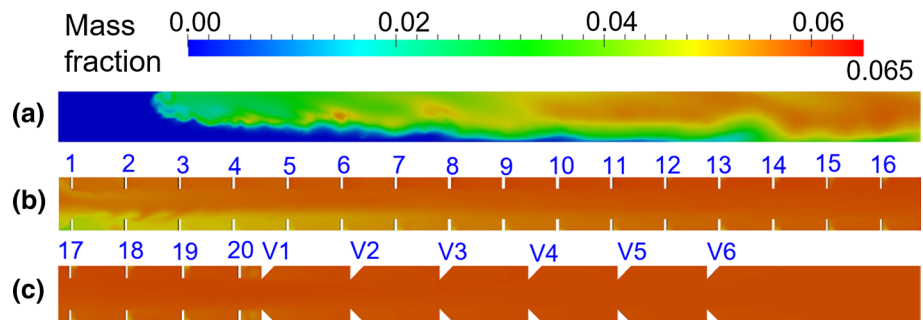
Figure 11 shows the temperature contour of the mixture with the existence of the fuel liquid droplets, while Fig. 12 only shows the fuel vapor mass fraction contour. Similarly, liquid droplets start to be vaporized immediately upon injection into the chamber. However, in this case, the liquid droplets exist and travel longer inside the detonation chamber; they even reach to the outlet of the detonation chamber (see Fig. 11). As such, the evaporation process occurs everywhere inside the detonation chamber during the droplet's movement. The mixture temperature is only slightly lower in the region after the injection point. And the fuel vapor mass fraction becomes greater toward the downstream end of the detonation chamber, since more fuel vapor is added to the mixture during the evaporation process of the droplets along their trajectory. Compared to the complete vaporization case above, it can be seen that both the temperature of the mixture and the fuel vapor mass fraction of this case are lower inside the detonation chamber.

In general, the droplet residence time (or the existence of the droplets inside the detonation chamber) is strongly dependent on the evaporation rate and incoming airflow velocity. When the temperature of the mixture surrounding the droplet is much greater than the saturation point, the evaporation rate is greater. Conversely, when the temperature of the surrounding mixture is closer to the saturation point, the evaporation rate becomes less. As mentioned before, both the evaporation rate and the surrounding temperature are affected by the inlet parameters and operating conditions. Thus, to attain the optimal evaporation process, one would need to control the inlet parameters and operating conditions. For example, if one wants to attain the fuel vapor/air equivalence ratio of about 1.0 for different global injected fuel/air equivalence ratios, one would have to control the temperature of airflow coming into the detonation chamber and/or control the incoming airflow velocity, etc.
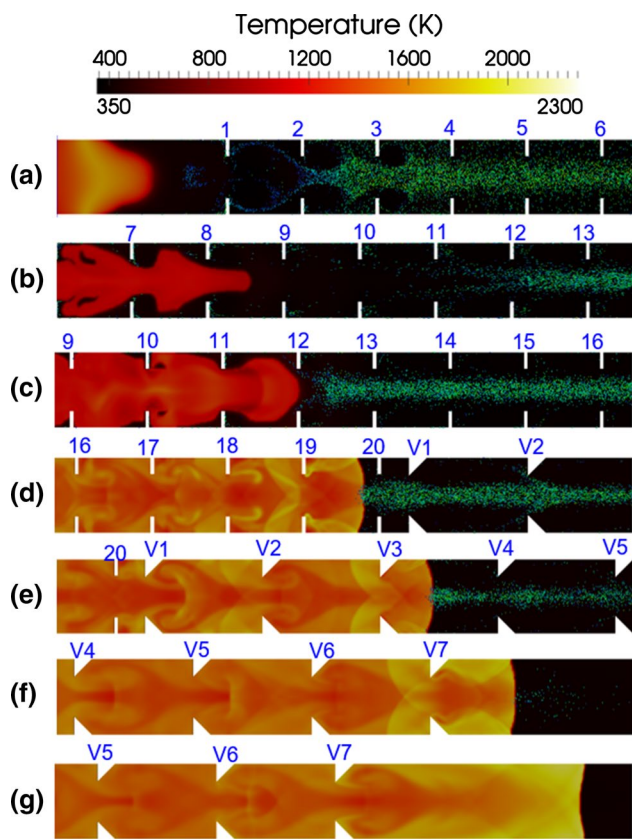
Fig. 13 Successful DDT process in the case of incomplete vaporization process; temperature contour is plotted at different times within the liquid droplets in green color at the unburnt region in front of the flame front
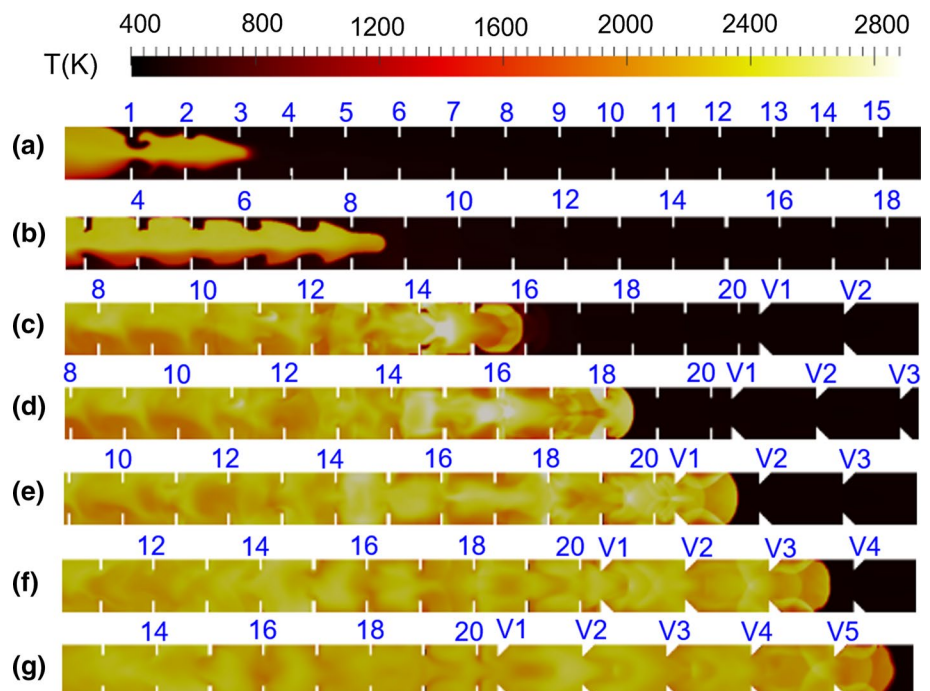
5.3 Successful DDT process in the completed/not completed evaporation

As mentioned in the previous section, the DDT process can successfully transit to detonation in both the complete and incomplete vaporization cases. In this section, the obtained numerical results are discussed and analyzed further. Figure 13 shows the successful DDT process in the incomplete vaporization case, while Fig. 14 shows the successful DDT process in the complete vaporization case.

In Fig. 13, the temperature contours are plotted at different times with the appearance of liquid droplets depicted in green color in the unburnt region. The flame is ignited using a small hot spot with high temperature at the ignition point. At the beginning, the flame is laminar and propagates at a very low speed in the downstream direction (as shown in Fig. 13a). It is clear that the liquid fuel droplets are completely evaporated in the region near the reaction front (flame front) due to the heat convection, advection, and radiation transferred from the vapor phase to the liquid droplets. The flame then accelerates inside the detonation chamber and becomes more turbulent under the effect of the orifice plates. Due to the expansion of the combustion products and advection, the liquid droplets are pushed in the downstream direction, broken up, and evaporated faster. This leads to a wider induction zone in front of the flame front (refer to Fig. 13b for details). The flame continues to accelerate inside the orifice plate region. The shock waves are then formed and so are the local hot spots. With the support from energy released from the combustion process under the effect of the shock waves, local hot spots, and compression waves,

Fig. 14 Successful DDT process in the case of complete vaporization process; temperature contour is plotted at different times with no liquid droplet at the unburnt region in front of the flame front

the reaction front (or flame front) propagates much faster (faster than the expansion wave and evaporation process). As such, the induction zone becomes smaller and smaller as in Fig. 13c. The detonation waves are formed as the reaction front approaches and couples with the shock front (see Fig. 13d for details). The detonation waves continue propagating toward the unburnt mixture, which contains the liquid fuel droplets (Fig. 13d–g). With a very thin induction zone, the remaining liquid droplets still exist inside the detonation region, but only in a very short time duration because of the very high temperature. The interaction between the detonation waves and liquid droplets results in a faster breakup and evaporation of the liquid droplets; however, it also results in a slowdown in the propagation speed of the detonation waves and a lower temperature of the combustion products. Finally, the detonation waves reach a stable state and travel at the C–J detonation velocity.

Figure 14 shows the successful DDT process in the complete vaporization case. The temperature contour is plotted at different times, but there is no appearance of the liquid-fueled droplet. Similarly, a laminar flame is ignited by a small local hot spot with high temperature at the ignition region. The laminar flame accelerates inside the orifice plate region (see Fig. 14a), the turbulence intensity increases, and compression and expansion waves are formed (see Fig. 14b) and shock waves are formed as well (see Fig. 4c). Then the local hot spots are observed, too. The flame front continues to accelerate and then reaches the shock front. As such, the detonation waves are formed as the flame front (reaction front) reaches and couples with the shock front (see Fig. 14d). Detonation waves continue propagating toward the unburnt mixture (see Fig. 14d–g). The detonation waves subsequently reach the stable state and travel at CJ speed. It may be noted that the DDT process in the pure gas mixture of fuel and air has been presented in many different previous studies (e.g., Nguyen et al. [43]), and hence, the details are not repeated in this work.

For the same global fuel/air equivalence ratio, comparing to the complete vaporization case, the maximum temperature of the detonation product mixture is much lower in the incomplete vaporization case. The maximum temperature is about 2800 K in the complete vaporization case, while it is about 2300 K in the incomplete vaporization case. Because, in the complete vaporization case, most of the chemical reactions occur at the region near the detonation front, and this leads to a huge amount of heat release in this area, and therefore, the temperature is very high. However, for the incomplete vaporization case, a lesser amount of fuel vapor will react with oxidizer in this region, which leads to a lesser amount of heat release. In addition, as the detonation waves propagate through the cold droplet region, the cold liquid droplets also take some heat from the detonation products due to the heat exchange, and as such the system is "cooled"

down. Some heat energy is added to the system due to the subsequent reactions of the new evaporating liquid droplets inside the detonation chamber. However, the total temperature in this case is still lower than the complete vaporization case. Similarly, both the flame propagation speed in the DDT process and the C–J detonation velocity in the incomplete vaporization case are also slightly lower than the complete vaporization case. This result can be explained through the interaction of the flame and/or detonation wave with the remaining liquid fuel droplets, the combustion product expansion, and the heat release.
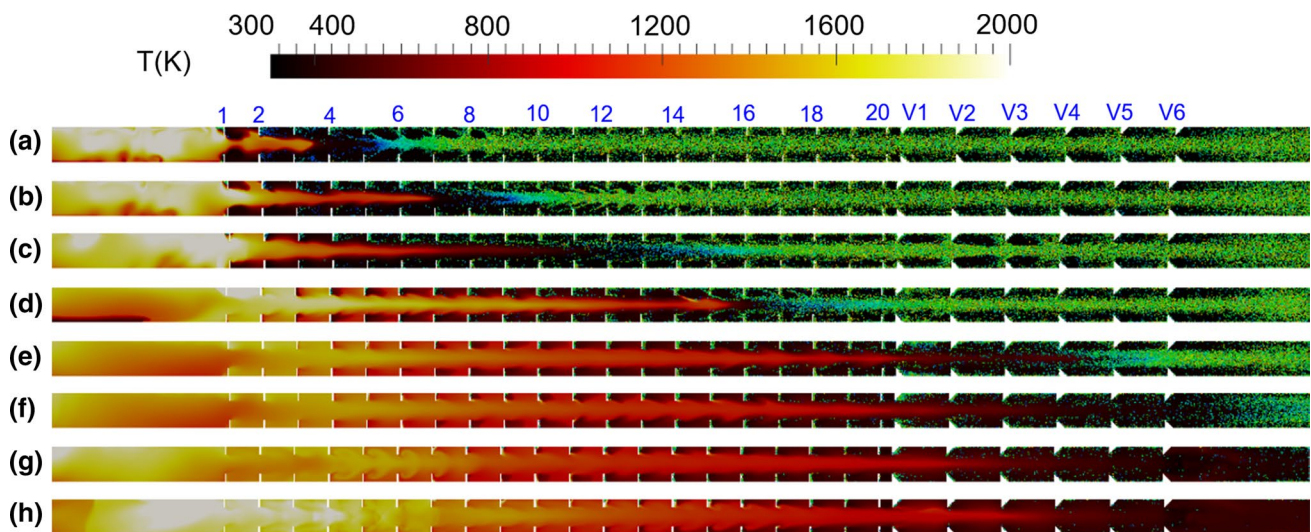
5.4 Unsuccessful DDT process

The case with injected liquid fuel at a mass flow rate of 2.5 g/s and a temperature of 300 K, and the incoming airflow at a temperature of 300 K and a velocity of 35 m/s in the OC2 case is used to demonstrate the unsuccessful DDT process. As mentioned in the previous section, this is an incomplete vaporization case and the fuel vapor mass fraction is only about 1.0×10^{-4} (equivalence ratio < 0.1). Figure 15 shows the temperature contours with the appearance of liquid droplets in green color at different times. The obtained numerical results show that the flame also accelerates inside the detonation chamber; however, weak shock waves, or even an absence of shock waves, and hot spots are formed. In other words, a lean pre-vaporized fuel can lead to a weaker and slower burning process. Hence, the energy released from that burning process is not instantly strong enough to generate a local hot spot or strong shock wave to form a detonation wave.

Upon careful examination, we found that the burning (reactions) occurs at two different stages. In the first burning stage, the oxidization only occurs between the pre-vaporization fuel vapor and oxidizer. Because the mass fraction of the pre-vaporization fuel vapor is very low (e.g., 1.0×10^{-4}), the heat release from chemical reactions are low. As a consequence, the temperature is relatively low in the burning region (e.g., the flame front) (about < 1000 K) (see Fig. 15). However, due to the expansion of the combustion products, the flame still propagates toward the unburnt region, which contains dense, cold liquid fuel droplets. As for staying inside the flame region, these liquid droplets continue to evaporate due to the high temperature of the surrounding gas phase. Changing from liquid phase to vapor phase also causes more expansion of the hot gas region, which then supports the flame front, pushing it faster.

This is the second burning stage which occurs inside the burning region of the first burning stage, where the remaining liquid droplets break up and evaporate completely under the interaction with the hot flame of the first burning stage. The high temperatures of the burning products start the second burning stage between the newly evaporated fuel

Fig. 15 Unsuccessful DDT process: temperature contour is plotted at different times within the liquid droplets depicted in green color at the unburnt region in front of the flame front

vapor and the remaining oxidizer. The heat release from the second burning stage makes the temperature of the mixture in this burning region higher (e.g., 2000 K) (see Fig. 15). The expansion of the hot burning products in the second stage then further pushes the flame front to move faster. The combination of the first and second burning stages causes stronger acceleration of the flame propagation. This may lead to the formation of weak shock waves or hot spots, but still not strong enough to form detonation waves. It should be noted that the amount of fuel pre-vaporization (the fuel vapor evaporated before ignition time) is very important to ensure the successful DDT process to transit to a detonation wave. The second burning step can only provide (secondary) support to the first burning step essential to attain a stronger shock waves or hot spots.

6 Conclusions

In this study, a computationally intensive numerical simulation platform based on the Eulerian–Lagrangian approach for the liquid-fueled PDE has been systematically implemented and validated against the relevant experimental data. The obtained numerical results are in good agreement with experimental data. The simulations were performed for the complete operating cycle of the PDE, which included the injection and evaporation process (stage 1), deflagration-to-detonation transition process (stage 2), and detonation wave propagation process (stage 3). The calculated flame propagation speed was comparable to the experimental results in the DDT process, while the numerical C–J detonation velocity was about 1800 m/s, which is close to the published and measured (experimental) data.

The simulations of the three inlet and operating condition sets are performed to explore further the influence of the operating conditions on all stages of the performance of the engine as well as the physical and chemical insights. The liquid fuel droplets can be completely or incompletely vaporized, which depends on the evaporation rate. The evaporation rate is affected by the surrounding vapor mixture temperature, which is strongly dependent on the inlet air flow temperature and operating conditions.

The DDT process can successfully transit to detonation waves in both the complete vaporization and incomplete vaporization cases. The pre-vaporization fuel vapor mass fraction (or fuel/air equivalence ratio) plays a very important role for the successful DDT process in liquid-fueled pulse detonation engines. There exists a certain range for the fuel vapor/air equivalence ratio (in this study, $\phi = 0.7$–2.35) for detonation onset, even for the fuel-rich case with global fuel/air equivalence ratio reaching a high value of 4.0. In addition, both the temperature and the C–J detonation velocity in the incomplete vaporization case are slightly lower than those in the complete vaporization case.

In the complete vaporization case, the burning process occurs in one stage and most of the chemical reactions occur in the region of the flame front, while in the incomplete vaporization case, the burning process occurs in two stages. In the first stage, the reactions only occur in the pre-vaporization fuel vapor with the surrounding air. In the second stage, the remaining liquid droplets are broken up and evaporated inside the burning region of the first stage; the newly vaporized fuel vapor then subsequently reacts with the remaining surrounding oxidizer. The temperature of the complete vaporization case is always greater than the incomplete vaporization case and is mainly focused in the region

near the flame front. Conversely, in the incomplete vaporization case, the temperature is lower at the flame front. The first burning stage plays the main role in the detonation onset, while the second stage only plays a secondary supporting role.

Appendix: Source term expressions

This section describes the sub-models for numerical source terms, which are described in the governing (1–4) for the vapor phase and (10–13) for the discrete phase. These source terms include the atomization model, injection model, dispersion model, drag model, heat transfer model, phase change model (evaporation model), and breakup model. The details are given as follows:

Atomization model

The atomization model supplies the initial conditions for spray computations (e.g., the droplet size, velocities, temperature, etc.) at the injector (nozzle) exit. In this study, the Linearized Instability Sheet Atomization model (LISA model) [44] is employed. In fact, the LISA atomization model is divided into three stages: (1) film formation, (2) sheet breakup, and (3) atomization. In the film formation stage, the thickness of the film, t, is related to the mass flow rate as in the following form:

$$\dot{m}_{\text{eff}} = \pi \rho u t \left(d_{\text{inj}} - t \right) \tag{15}$$

where d_{inj} is the injector exit diameter, $\dot{m}_{\text{eff}}$ is effective mass flow rate (mass flow rate/discharge coefficient), ρ is liquid fuel density, and velocity is determined as $u = U\cos\theta$ with θ is the spray angle. Total velocity, U, is defined as $U = C_{\text{d}}\sqrt{\frac{2(P_{\text{inj}} - P_{\text{ambient}})}{\rho}}$ where C_{d} is the discharge coefficient; P_{inj} is the injection pressure; and P_{ambient} is the ambient pressure.

In the sheet breakup stage, the model often includes the effects of the surrounding gas, liquid viscosity, and surface tension on the breakup of the liquid sheet. Details of the theoretical development of the model are given in Senecal et al. [45] and are only briefly presented here. The breakup from ligaments to droplets is assumed to behave according to the analysis of Weber et al. [46] for capillary instability as

$$d_0 = 1.88 d_{\text{L}} (1 + 3\,\text{Oh})^{1/6}. \tag{16}$$

Here, Oh is the Ohnesorge number, which is a combination of the Reynolds number and the Weber number [47]. d_0 is initial droplet, which is assumed that this droplet diameter is the most probable droplet size of the Rosin–Rammler distribution.

For the atomization stage, the calculation concerns secondary atomization, aerodynamic drag, collisions, and coalescence. The aerodynamic drag is calculated with the drag and distortion. Turbulence drop-dispersion effects are also included. In this study, the turbulence model is the k–ω SST model. The occurrence of collisions and coalescence can be computed according to O'Rourke [48]; however, they are not accounted for in this study.

Breakup modeling

For the breakup regimes of liquid droplets, aerodynamic forces, induced by the relative velocity between droplets and surrounding gas, act on the droplet's surface. These forces result in the unstable growth of waves on the surface or the whole droplet itself. The growing waves lead to a breakup or disintegration of the droplet to form smaller droplets if the surface tension is not high enough to stabilize the droplet. The ratio of the aerodynamic force to surface tension force is described by the Weber number, $\text{We} = \rho d u^2 / \sigma$ where d is droplet diameter, ρ is gas density, u is the relative velocity between droplet and surrounding gas, and σ is the surface tension force. Experiments have shown that the breakup mode changes with growing Weber number [47]: vibrational mode ($\text{We} \leq 12$), Bag mode ($\text{We} < 20$), Bag-streamer ($\text{We} < 50$), Stripping ($\text{We} < 100$), and Catastrophic ($\text{We} > 100$). For the primary breakup model, the continuous liquid core of the jet is designated into several discrete droplets after the primary breakup; this is enforced by the flow condition inside the nozzle hole. Since the continuous liquid phase cannot be represented using the Lagrangian description, this primary breakup model cannot be simulated directly. This is often treated separately based on the injection conditions (injection pressure, injection mass flow rate, and size of injection hole) to determine the initial conditions for the droplets (e.g., initial droplet size, initial velocity, initial temperature, number of the droplets, cone angle, etc.).

For modeling of the secondary and subsequent breakups, in this study, a combined breakup model is used to improve upon the accuracy of the breakup prediction since there is no single breakup model suitable for all flow regimes. Thus, the Rayleigh–Taylor and Kelvin–Helmholtz breakup model (RT–KH breakup model) is implemented in the simulation platform [49, 50]. The Kelvin–Helmholtz breakup model [49] is often used to model the separation of small droplets from the initial drop. The model assumes that the breakup is caused by Kelvin–Helmholtz instability. These instabilities occur because of the velocity difference between the droplet and surrounding gas. The waves with the highest growth rate will be sheared off to form new droplets. The solution for the maximum wave growth rate is given as

$$\Omega = \frac{0.34 + 0.38\text{We}^{1.5}}{(1 + Z)(1 + 1.4T^{0.6})}\sqrt{\frac{\sigma}{\rho_\ell r_0^3}} \qquad (17)$$

where $Z = \sqrt{\text{We}}/\text{Re}_\ell$, and $T = Z\sqrt{\text{We}_g}$ with the liquid Reynolds number and gaseous Weber number. The corresponding wavelength is expressed as

$$\frac{\Lambda}{r_0} = 9.02\frac{(1 + 0.45Z^{0.5})(1 + 0.4T^{0.7})}{(1 + 0.865\text{We}_g^{1.67})^{0.6}}. \qquad (18)$$

The size of the separation droplet depends on the wavelength Λ since the new droplets are formed by the oscillation. Thus, the size of the new droplet can be estimated as

$$r_{\text{new}} = B_0\Lambda \qquad (19)$$

with constant $B_0 = 0.61$. The new droplets with radius r_{new} are inserted next to the parent droplets. To enforce the mass conservation, the size of the droplet has to decrease for the same mass lost to the new droplets.

The disintegration of the droplets in the catastrophic breakup regimes (We > 100) is modeled by the Rayleigh–Taylor breakup model [50]. The droplets are decelerated by aerodynamic forces induced by relative velocity between droplet and surrounding gas. The drag force acts on the front side of the droplet with density ρ_ℓ and radius r with deceleration rate as

$$a = \frac{3}{8}\pi C_D\frac{\rho_g u_{\text{rel}}^2}{\rho_\ell r}. \qquad (20)$$

In this expression, C_D represents the drag coefficient and u_{rel} is the relative velocity. Due to the inertia force, the backside of the droplet does not decelerate as fast as the front side; thus, new droplets are formed. It is assumed that the breakup is initiated by the waves with the fastest growth. The wavelength with fastest growth can be expressed as

$$\Lambda_{\text{RT}} = 2\pi C_3\sqrt{\frac{\sigma}{a(\rho_\ell - \rho_g)}}. \qquad (21)$$

The corresponding growth is given by

$$\Omega_{\text{RT}} = \sqrt{\frac{2}{3\sqrt{3}\sigma}\frac{[a(\rho_\ell - \rho_g)]^{3/2}}{\rho_\ell + \rho_g}}. \qquad (22)$$

During the breakup process, the parent droplet is replaced by smaller droplets at time $t = \Omega_{\text{RT}}$. The number of the new droplets are determined by the ratio of the maximum diameter of the deformed parent droplet to Λ_{RT}. The radius of the new droplets is determined using the conservation of mass.

Heat transfer model

In this study, the Ranz–Marshall heat transfer model [22, 23] is used to account for the heat transfer from liquid fuel droplet to the surrounding gas, and vice versa. This model is based on the convective heat transfer of the droplet with uniform temperature. A modification is implemented to account for the latent heat phase transfer during the evaporation process. The heat transfer model also uses the evaporation relaxation time, since the evaporation of the droplet also transfers heat to the surrounding gas. That is

$$\frac{dT_d}{dt} = \frac{\pi D\kappa_c\text{Nu}}{m_d c_\ell}(T_g - T_d)f_{\text{heat}} - \frac{1}{c_\ell}\frac{h_v(T_d)}{\tau_e}. \qquad (23)$$

The modification is implemented in the factor f_{heat} as the following:

$$f_{\text{heat}} = \frac{-\frac{c_{p,v}\dot{m}_d}{\pi D\kappa_c\text{Nu}}}{e^{-\left(\frac{c_{p,v}\dot{m}_d}{\pi D\kappa_c\text{Nu}}\right)} - 1}. \qquad (24)$$

In this expression, the first part of the equation accounts for the heat transfer from the surrounding gas to the liquid droplet, while the second part represents the latent heat arising from mass transfer. D is diameter of the droplet, κ_c is the heat transfer coefficient, Nu is the Nusselt number, T_g is the surrounding gas temperature, T_d is the droplet temperature, m_d is the droplet mass, and h_v is the droplet enthalpy.

Evaporation model

In the modeling of the fuel evaporation, the key parameter is the lifetime (or evaporation relaxation time) of the droplet [25]. The derivation of this time starts by evaluating the time derivative of the mass of the droplet:

$$\frac{dm_d}{dt} = \rho_d\frac{d}{dt}\left(\frac{4}{3}\pi\left(\frac{D}{2}\right)^3\right) = \frac{\pi\rho_d}{2}D^2\frac{dD}{dt}. \qquad (25)$$

The evaporation time is assumed to follow the empirical D^2-law given as:

$$\frac{dD^2}{dt} = C_e \rightarrow \frac{dD}{dt} = \frac{C_e}{2D} \qquad (26)$$

where C_e is a constant. From this equation, we can determine the relaxation time by integration as the following:

$$D^2 = C_e t + D_0^2. \qquad (27)$$

The time life is determined as the droplet completely evaporated from the original droplet size (D_0) as follows:

$$\tau_e = -\frac{D_0^2}{C_e}. \tag{28}$$

The coefficient C_e is given by

$$C_e = -4\text{Sh}\frac{\rho_g}{\rho_d}D\ln\left(1 + \frac{X_{v,s} - X_{v,inf}}{1 - X_{v,s}}\right) \tag{29}$$

with Sherwood number (Sh) calculated as the following Ranz–Marshall correlation [22, 23]:

$$\text{Sh} = 2 + 0.6\text{Re}^{1/2}\text{Sc}^{1/3}. \tag{30}$$

It should be noted that the evaporation model (phase change model) must satisfy the mass conservation law.

Momentum source term

The momentum source term ($S_{d,u} = -S_{g,u}$) for the two-way interaction between the gas phase and the solid particles shown in (2) and (11) can be expressed as flows:

$$S_{d,u} = F_D(\boldsymbol{u}_g - \boldsymbol{u}_p) + F_g + F_p + \frac{\partial m_d}{\partial t}\boldsymbol{u}_d. \tag{31}$$

In this expression, the forces are the drag force (F_D), gravity force (F_g), pressure gradient force (F_p), and the added mass force ($\frac{\partial m_d}{\partial t}\boldsymbol{u}_d$). $\boldsymbol{u}_g$ is the velocity of the gas field. $\boldsymbol{u}_d$ is velocity of the droplet. $\frac{\partial m_d}{\partial t}$ is the change in droplet mass. The drag force is defined as

$$F_D = \frac{\pi d_d^2}{8}\rho_g C_D\left|\boldsymbol{u}_g - \boldsymbol{u}_d\right|, \tag{32}$$

where d_d is the particle diameter, ρ_g is the density of the gas mixture, and C_D is the drag coefficient. The modified Schiller–Naumann correlation [51] is used to evaluate the drag coefficient:

$$C_D = \begin{cases} \frac{24}{\text{Re}_p}\left(1 + 0.15\text{Re}_p^{0.687}\right) & \text{for } \text{Re}_p \leq 1000 \\ 0.44 & \text{for } \text{Re}_p > 1000 \end{cases} \tag{33}$$

with the Reynolds number defined as $\text{Re}_p = \frac{\rho_g d_p}{\mu_g}\left|\boldsymbol{u}_g - \boldsymbol{u}_p\right|$. μ_g is the dynamic viscosity of the gas mixture.

The pressure gradient force acting on the particle is defined as:

$$F_p = V\nabla p = \rho_g V\left(\frac{D\boldsymbol{u}_g}{Dt} - \nu\nabla^2\boldsymbol{u}_g\right) \tag{34}$$

with V as the particle volume, ∇p is the pressure gradient, and ν is the kinetic viscosity of the gas mixture. It should be

noted that the added mass is very small compared to other forces in (31), so that it is omitted in this study.

Droplet mass source term

The droplet mass source term (S_{md}) in (14) is the change in single droplet mass, which is equaled to the amount of vaporization and breakup. Mass change due to vaporization is defined as

$$S_{md} = \pi\rho_d\frac{4}{3}\left(\left(\frac{d_d^n}{2}\right)^3 - \left(\frac{d_d^{n+1}}{2}\right)^3\right). \tag{35}$$

In (35), ρ_d is the liquid fuel density, d_d^n is the diameter of the liquid droplet at time t^n, and d_d^{n+1} is the diameter of the liquid droplet at time $t = t^n + dt$. Mass change due to the breakup is defined as

$$\pi\rho_d\frac{4}{3}\left(\frac{d_d^n}{2}\right)^3 = \sum_{i=1}^{N}\pi\rho_d\frac{4}{3}\left(\frac{d_{d,i}^{n+1}}{2}\right)^3. \tag{36}$$

In (36), N is the total number of droplets created after the breakup. $d_{d,i}$ is the diameter of the droplet i.

References

1. Kailasanath, K.: Recent developments in the research on pulse detonation engines. AIAA J. **41**, 145–159 (2003). https://doi.org/10.2514/2.1933
2. Webber, W.F.: Spray combustion in the presence of a travelling wave. Symp. (Int.) Combust. **8**, 1129–1140 (1961). https://doi.org/10.1016/S0082-0784(06)80611-9
3. Cramer, F.B.: The onset of detonation in droplet combustion field. Symp. (Int.) Combust. **9**, 482–484 (1963). https://doi.org/10.1016/S0082-0784(63)80058-2
4. Ragland, K.W., Dabora, E.K., Nicholls, J.A.: Observed structure of spray detonation. Phys. Fluids **11**, 2377–2389 (1968). https://doi.org/10.1063/1.1691827
5. Dabora, E.K., Ragland, K.W., Nicholls, J.A.: Droplet-size effects in spray detonations. Symp. (Int.) Combust. **12**, 19–26 (1969). https://doi.org/10.1016/S0082-0784(69)80388-7
6. Bull, D.C., McLeod, M.A., Minzer, G.A.: Detonation of unconfined fuel aerosols. Prog. Astronaut. Aeronaut. **75**, 48–60 (1981). https://doi.org/10.2514/5.9781600865497.0048.0060
7. Brophy, C.M., Netzer, D.W., Sinibali, J., Johnson, R.: Detonation of JP-10 aerosol for pulse detonation engine applications. In: Roy, G.D., Frolov, S.M., Netzer, D.W., Borisov, A.A. (eds.) High-Speed Deflagration and Detonation, pp. 207–222. ELEX-KM Publishers, Moscow (2001)
8. Frolov, S.M.: Liquid-fueled, air-breathing pulse detonation engine demonstrator: operation principles and performances. J. Propuls. Power **22**(6), 1162–1169 (2006). https://doi.org/10.2514/1.17968
9. Fan, W., Yan, C., Huang, X., Zhang, Q., Zheng, L.: Experimental investigation of two-phase detonation engine. Combust. Flame **133**(4), 441–450 (2003). https://doi.org/10.1016/S0010-2180(03)00043-9

10. Schauer, F.R., Miser, C.L., Tucker, K.C., Bradley, R.P., Hoke, J.L.: Detonation initiation of hydrocarbon-air mixture in pulse detonation engine. 43rd AIAA Aerospace Sciences Meeting and Exhibit, Reno, NV. AIAA Paper 2005-1343 (2005). https://doi.org/10.2514/6.2005-1343

11. Tucker, K.C., King, P.I., Schauer, F.R.: Hydrocarbon fuel flash vaporization for pulse detonation combustion. J. Propuls. Power 24(4), 788–796 (2008). https://doi.org/10.2514/1.28412

12. Li, J.M., Teo, C.J., Chang, P.H., Li, L., Lim, K.S., Khoo, B.C.: Excessively fuel rich conditions for cold starting of liquid fueled pulse detonation engines. J. Propuls. Power 33(1), 71–79 (2017). https://doi.org/10.2514/1.B36088

13. Williams, F.A.: Structure of detonation in diluted sprays. Phys. Fluids 4, 1434–1443 (1961). https://doi.org/10.1063/1.1706236

14. Borisov, A.A., Gelfand, B.E., Gubin, S.A., Kogarko, S.M., Podgrebenkov, A.L.: The reaction zone of two-phase detonations. Astronaut. Acta 15, 411–417 (1970)

15. Burcat, A., Eidelman, S.: Evolution of the detonation wave in a cloud of fuel droplets: Part II. Influence of fuel droplets. AIAA J. 18, 1233–1236 (1980). https://doi.org/10.2514/3.7717

16. Chang, E.J., Kailasanath, K.: Shock wave interactions with particles and fuel droplets. Shock Waves 12, 333–341 (2003). https://doi.org/10.1007/s00193-002-0170-1

17. Cheatham, S., Kailasanath, K.: Numerical modelling of liquid-fuelled detonation in tubes. J. Combust. Theory Model. 9, 23–48 (2005). https://doi.org/10.1080/13647830500051786

18. Miller, R.S., Bellan, J.: Direct numerical simulation of the confined three-dimensional gas mixing layer with one evaporating hydrocarbon-droplet-laden stream. J. Fluid Mech. 384, 293–338 (1999). https://doi.org/10.1017/S0022112098004042

19. Aggarwal, S.K., Peng, F.: A review of droplet dynamics and evaporation modelling for engineering calculations. J. Eng. Gas Turbines Power 117, 453–460 (1995). https://doi.org/10.1115/1.2814117

20. Gubin, S.A., Sichel, M.: Calculation of detonation velocity of a mixture of liquid fuel droplet and gas oxidizer. Combust. Sci. Technol. 17, 109–117 (1977). https://doi.org/10.1080/00102207708946821

21. Nguyen, V.B., Li, J.M., Chang, P.H., Phan, Q.T., Teo, C.J., Khoo, B.C.: On the deflagration-to-detonation transition (DDT) process with added energetic solid particles for pulse detonation engines (PDE). Shock Waves 28(6), 1143–1167 (2018). https://doi.org/10.1007/s00193-017-0800-2

22. Ranz, W.E., Marshall, W.R.: Evaporation from drops. Part I. Chem. Eng. Prog. 48(3), 141–146 (1952)

23. Ranz, W.E., Marshall, W.R.: Evaporation from drops. Part II. Chem. Eng. Prog. 48(4), 173–180 (1952)

24. Liu, A.B., Mather, D., Reitz, R.D.: Modeling the effects of drop drag and breakup on fuel sprays. SAE Technical Paper 930072. SAE (1993). https://doi.org/10.4271/930072

25. Law, C.K., Law, H.K.: A d^2-law for multicomponent droplet vaporization and combustion. AIAA J. 20(4), 522–527 (1982). https://doi.org/10.2514/3.51103

26. Ajmani, K., Kundu, K., Penko, P.: A study on detonation of Jet-A using a reduced mechanism. 48th AIAA Aerospace Sciences Meeting Including the New Horizons Forum and Aerospace Exposition, Orlando, FL. AIAA Paper 2010-1515 (2010). https://doi.org/10.2514/6.2010-1515

27. Menter, F.R.: Two-equation eddy-viscosity turbulence models for engineering applications. AIAA J. 32(8), 1598–1605 (1994). https://doi.org/10.2514/3.12149

28. Launder, B.E., Sharma, B.I.: Application of the energy dissipation model of turbulence to the calculation of flow near a spinning disc. Lett. Heat Mass Transf. 1(2), 131–138 (1974). https://doi.org/10.1016/0094-4548(74)90150-7

29. Wilcox, D.C.: Formulation of the k–ω turbulence model revisited. AIAA J. 46(11), 2823–2838 (2008). https://doi.org/10.2514/1.36541

30. Henry, W., et al.: OpenFOAM User Guide, Version 2.1.x. The OpenFOAM Foundation (2012). http://www.openfoam.org

31. Menter, F.R., Kuntz, M., Langtry, R.: Ten years of industrial experience with the SST turbulence model. Turbul. Heat Mass Transf. 4, 624–632 (2003)

32. Kuensberg, S.C., Kong, S.-C., Reitz, R.D.: Modelling the effects of injector nozzle geometry on diesel sprays. SAE Paper 1999-01-0912 (1999). https://doi.org/10.4271/1999-01-0912

33. Kee, R.J., Rupley, F.M., Miller, J.A., et al.: The CHEMKIN thermodynamic database, CHEMKIN Collection, release 3.6 (2000). http://www.sandia.gov/chemkin

34. Bird, R.B., Stewart, W.E., Lightfoot, E.N.: Transport Phenomena. Wiley, New York (2001)

35. Bray, K.N.C., Moss, J.B.: A unified statistical model of the premixed turbulent flame. Acta Astronaut. 4(3–4), 291–319 (1977). https://doi.org/10.1016/0094-5765(77)90053-4

36. Turns, S.R.: An Introduction to Combustion: Concepts and Applications, 3rd edn. McGraw-Hill, New Delhi (2000)

37. Weller, H.G., Tabor, G., Gosman, A.D., Fureby, C.: Application of a flame-wrinkling LES combustion model to a turbulent mixing layer. Int. Symp. Combust. 27, 899–907 (1998). https://doi.org/10.1016/S0082-0784(98)80487-6

38. Ettner, F., Vollmer, K.G., Sattelmayer, T.: Numerical simulation of the deflagration-to-detonation transition in inhomogeneous mixtures. J. Combust. 2014, 686347 (2014). https://doi.org/10.1155/2014/686347

39. Toro, E.F., Spruce, M., Spears, W.: Restoration of the contact surface in the HLL-Riemann solver. Shock Waves 4(1), 25–34 (1994). https://doi.org/10.1007/BF01414629

40. OpenFOAM Wiki Limiters (2010). http://openfoamwiki.net/index.php/OpenFOAM_guide/Limiters

41. Migdal, D., Agosta, V.: A source flow model for continuum gas-particle flow. J. Appl. Mech. 34(4), 860–865 (1967). https://doi.org/10.1115/1.3607848

42. Baseline Spray A: non-reacting conditions, ECN Workshop 1, May 2011. http://public.ca.sandia.gov/ecn/cvdata/targetCondition/sprayA.php

43. Nguyen, V.B., Li, J.M., Chang, P.H., Teo, C.J., Khoo, B.C.: Effect of ethylene fuel/air equivalence ratio on the dynamics of deflagration-to-detonation transition and detonation propagation process. Combust. Sci. Technol. 190(9), 1630–1658 (2018). https://doi.org/10.1080/00102202.2018.1461091

44. Schmidt, D.P., Nouar, I., Senecal, K.K., Rutland, C.J., Martin, J.K., Reitz, R.D.: Pressure-swirl atomization in the near field. SAE Paper 01-0496. SAE (1999). https://doi.org/10.4271/1999-01-0496

45. Senecal, P.K., Schmidt, D.P., Nouar, I., Rutland, C.J., Reitz, R.D., Corradini, M.: Modeling high speed viscous liquid sheet atomization. Int. J. Multiph. Flow 25, 1073–1097 (1999). https://doi.org/10.1016/S0301-9322(99)00057-9

46. Weber, C.: For the decay of a liquid jet. ZAMM 11, 136–154 (1931). https://doi.org/10.1002/zamm.19310110207

47. Ohnesorge, W.: Formation of drops by nozzles and the breakup of liquid jets. J. Appl. Math. Mech. 16, 355–358 (1936)

48. O'Rourke, P.J., Amsden, A.A.: The TAB method for numerical calculation of spray droplet breakup. SAE Technical Paper 872089. SAE (1987). https://doi.org/10.4271/872089

49. Reitz, R.D.: Mechanisms of atomization processes in high-pressure vaporizing sprays. At. Spray Technol. 3, 309–337 (1987)

50. Beale, J.C., Reitz, R.D.: Modeling spray atomization with the Kelvin–Helmholtz/Rayleigh–Taylor hybrid model. At. Sprays 9, 623–650 (1999). https://doi.org/10.1615/AtomizSpr.v9.i6.40

51. Schiller, L., Naumann, A.: A drag coefficient correlation. Z. Ver. Dtsch. Ing. 77, 318–320 (1935)